nature communications

Article

https://doi.org/10.1038/s41467-024-54557-8

Modularity-based mathematical modeling of ligand inter-nanocluster connectivity for unraveling reversible stem cell regulation

Received: 1 September 2023

Accepted: 14 November 2024

Published online: 23 December 2024

Check for updates

Chowon Kim[1,18], Nayeon Kang[1,18], Sunhong Min[1], Ramar Thangam[1], Sungkyu Lee[1], Hyunsik Hong[1], Kanghyeon Kim[1], Seong Yeol Kim[1], Dahee Kim[1], Hyunji Rha[1], Kyong-Ryol Tag[1,2], Hyun-Jeong Lee[1,2], Nem Singh[1,3], Daun Jeong[4], Jangsun Hwang[4], Yuri Kim[1], Sangwoo Park[1], Hyesung Lee[5], Taeeon Kim[6,7], Sang Wook Son[8], Steve Park[9], Solmaz Karamikamkar[10], Yangzhi Zhu[10], Alireza Hassani Najafabadi[10], Zhiqin Chu[11], Wujin Sun[12], Pengchao Zhao[13], Kunyu Zhang[13], Liming Bian[13], Hyun-Cheol Song[14,15], Sung-Gyu Park[6,7], Jong Seung Kim[3], Sang-Yup Lee[5], Jae-Pyoung Ahn[2], Hong-Kyu Kim[2], Yu Shrike Zhang[16] ✉ & Heemin Kang[1,7,17] ✉

The native extracellular matrix is continuously remodeled to form complex interconnected network structures that reversibly regulate stem cell behaviors. Both regulation and understanding of its intricate dynamicity can help to modulate numerous cell behaviors. However, neither of these has yet been achieved due to the lack of designing and modeling such complex structures with dynamic controllability. Here we report modularity-based mathematical modeling of extracellular matrix-emulating ligand inter-cluster connectivity using the graph theory. Increasing anisotropy of magnetic nano-blockers proportionately disconnects arginine-glycine-aspartic acid ligand-to-ligand interconnections and decreases the number of ligand inter-cluster edges. This phenomenon deactivates stem cells, which can be partly activated by linearizing the nano-blockers. Remote cyclic elevation of high-anisotropy nano-blockers flexibly generates nano-gaps under the nano-blockers and augments the number of ligand inter-cluster edges. Subsequently, integrin-presenting stem cell infiltration is stimulated, which reversibly intensifies focal adhesion and mechanotransduction-driven differentiation both in vitro and in vivo. Designing and systemically modeling extracellular matrix-mimetic geometries opens avenues for unraveling dynamic cell-material interactions for tissue regeneration.

Remodeling of the native extracellular matrix (ECM) to reversibly establish connections therein orchestrates the dynamic function of the ECM to regulate cell behaviors[1]. Traumatic injury, such as bone fracturing, disconnects a tissue structure, which then requires reconnection by regulating the mechanotransduction and differentiation of stem cells[2–4]. Tendons, which are a type of connective tissue, contain a fibrillar collagen network that continuously connects and disconnects the muscle and the bone to regulate its physiological mechanical function and pathological process[5]. The connectivity in tissues and organs plays a crucial role in determining their function where the

A full list of affiliations appears at the end of the paper. ✉e-mail: yszhang@bwh.harvard.edu; heeminkang@korea.ac.kr

disconnection at specific sites can affect their physiology and pathology[6–9]. For example, the disconnection, reconnection, and extension of blood vessels critically regulate systemic blood flow and physiology[10]. The disconnection of periodontal ligament fibers attached to the root surfaces of teeth signifies periodontitis[11]. Disconnections between the axons[12] in the brain tissue can be caused by traumatic brain injury and diseases, such as Rasmussen syndrome[13]. The mapping of network interconnectivity in the brain tissue to understand the relationship between its structure and pathology has been attempted, albeit without their active regulation or modeling of its structure[14]. These prior findings collectively suggest the intricate and dynamic nature of ECM interconnectivity, which necessitates the development and modeling of interconnectivity-regulating materials to systematically unravel the effect of regulating material interconnectivity on stem cell behaviors that can assist tissue regeneration[15–20].

Meanwhile, the graph theory, which can quantify the interconnectivity of a network, has recently been highlighted for calculating the complex nanostructures of materials composed of interconnected building blocks[21] and interconnected networks of various cell types[22,23]. The Louvain algorithm is employed in graph theory to determine the optimal partition of clusters using modularity by maximizing intra-cluster connectivity while minimizing inter-cluster connectivity[24]. The cluster partition with modularity can help to discern formed clusters within a network and quantify the inter-cluster connectivity between them as the number of inter-cluster edges[25,26]. Therefore, graph theory, such as the Louvain algorithm, which allows for the mathematical modeling of interconnected networks, can be harnessed to realize the systematic analysis of how inter-cluster connectivity in materials governs cell behaviors.

Materials displaying various ligand configurations have recently been developed. To this end, different parameters of ligand configurations, such as varying their density and spacing[27], micropatterning[28,29], multivalency[30], and clustering[31], have been examined to determine their effects on cell behaviors. In particular, it has recently been shown that bridging between one-dimensional (1-D) fiber-like ligands can modulate cell behaviors[32]. Furthermore, integrin-binding ligands, such as arginine-glycine-aspartic acid (RGD) can mediate cellular filopodia formation, thereby driving focal adhesion and mechanotransduction that regulates the behaviors of stem cells, which is beneficial for tissue regeneration[33–35]. The shape tuning of molecules[30] or patterns[28] of protein ligands has been found to modulate stem cell differentiation. Going further, 1-D shape tuning of stem cells has recently been reported to trigger mechanotransduction signaling for functional tissue regeneration and organoid formation[36]. However, in all of these examples, ligand interconnectivity was not modulated due to the inability to block neighboring ligand connections which thus yielded entirely interconnected ligands, thereby suggesting the necessity for the design of sophisticated materials.

Furthermore, adapting a mathematical model to systemically analyze dynamic ligand inter-cluster connectivity in terms of # ligand inter-cluster edges tremendously helps establish realistic models since the native ECM undergoes dynamic remodeling that reversibly connects and disconnects its network structure to regulate cell behaviors[1]. Such dynamic modeling necessitates the design of materials that can be reversibly regulated, preferably via remote stimuli[37–39]. Compared with light-based stimuli that entail inevitable absorption by tissues depending on their wavelength[40–44], a magnetic field can readily penetrate tissues with negligible absorption[45–47] and thus be intensively applied for patients without any deleterious effects[48,49]. However, none of the recent reports including our and other groups harnessing remote stimuli such as the light-based control of the swelling of ligand microgels[41] and ligand exposure[40,42,50], as well as magnetic field-based control of 1-D nano-helical ligand stretching[51] and 1-D nano-sequenced ligand alignment[52] have used mathematical modeling to analyze the modulation of ligand blocking to regulate ligand interconnectivity.

Herein, we present mathematical modeling of ECM-emulating ligand inter-cluster connectivity using the graph theory (Fig. 1). The 1-D anisotropic-shaped magnetic nano-blockers obstruct the interconnection between RGD ligand nodes that are uniformly arranged, enabling the anisotropy-dependent reduction of the average number of ligand inter-cluster edges (referred as "# ligand inter-cluster edges") without changing the ligand density. High anisotropy of nano-blockers ("High aniso.") efficiently obstructs the interconnection between ligand clusters, which are divided based on the Louvain algorithm, and thus yields a low # ligand inter-cluster edges, which suppresses stem cell adhesion and differentiation. In contrast, low anisotropy of nano-blockers ("Low aniso.") inefficiently obstructs the interconnection of ligand clusters that produce high # inter-cluster edges, thereby stimulating focal adhesion and mechanotransduction of stem cells toward reinforcing their differentiation, both in vitro and in vivo. Moreover, we demonstrate that # ligand inter-cluster edges can be remotely manipulated using a magnetic field (Fig. 2). Randomly arranged high-anisotropy nano-blockers can be magnetically directed to be linearly ordered that partially enables local interconnections between the ligand nodes "High aniso. (Lin.)", consequently enhancing # ligand inter-cluster edges to some extent. High-anisotropy nano-blockers grafted to the surface of material via polymer linkers are originally in the non-elevated state ("NE.") and can be magnetically elevated ("E.") to facilitate the reconnection of the ligand nodes, thereby allowing cellular filopodia to infiltrate under the elevated nano-blockers, which significantly escalates # ligand inter-cluster edges. Strikingly, this transition can be repeatedly modulated to enable cyclic elevation that reversibly stimulates integrin-presenting filopodia formation of stem cells along with their focal adhesion and mechanosensing-mediated differentiation.

Our present study of employing 1-D anisotropic-shaped magnetic nano-blockers to regulate # inter-cluster edges of the interconnected ligands can dynamically regulate cell behaviors. The mathematical model for interconnectivity-regulating materials in the present study could be broadly beneficial for mimicking the dynamic and complex features of ECM interconnectivity, thereby unraveling the regulatory mechanism of stem cell behaviors for tissue-regenerative therapies.

Results

In situ phase transformation of anisotropic nano-blockers

For reversible tuning of the average number of inter-cluster edges (referred to as "# inter-cluster edges") within interconnected ligand networks, in situ phase transformation was strategically employed to fabricate magnetically reversible nano-blockers. To this end, akaganeite (β-ferric oxyhydroxide) nanorods with various dimensions as the core of nano-blocker precursors were first prepared by regulating the concentration of iron(III) chloride via a hydrolysis process with a high concentration yielding high anisotropy in the akaganeite nanorods. The nanorods were then encapsulated in silica envelops (anisotropic nano-blocker precursors) to optimize their projected area to be similar at varied anisotropies (low, moderate, and high). The low-magnification transmission electron microscopy (TEM) images verified the homogeneous shape of the nano-blocker precursors (Supplementary Fig. 1). The high-angle annular dark-field scanning TEM (HAADF-STEM) images and energy dispersive spectroscopy (EDS) mapping profiles confirmed the uniform presence of Fe element in the akaganeite core and Si element in the silica envelop, while O element was uniformly present in both of them (Supplementary Fig. 1). Crystalline atomic structure analysis of the nano-blocker precursors via high-resolution TEM (HR-TEM) images with respective fast Fourier transform (FFT) analysis and selected area diffraction (SAD) pattern imaging confirmed the presence of the akaganeite phase in all their cores regardless of the varied anisotropy (Supplementary Fig. 2).

https://doi.org/10.1038/s41467-024-54557-8

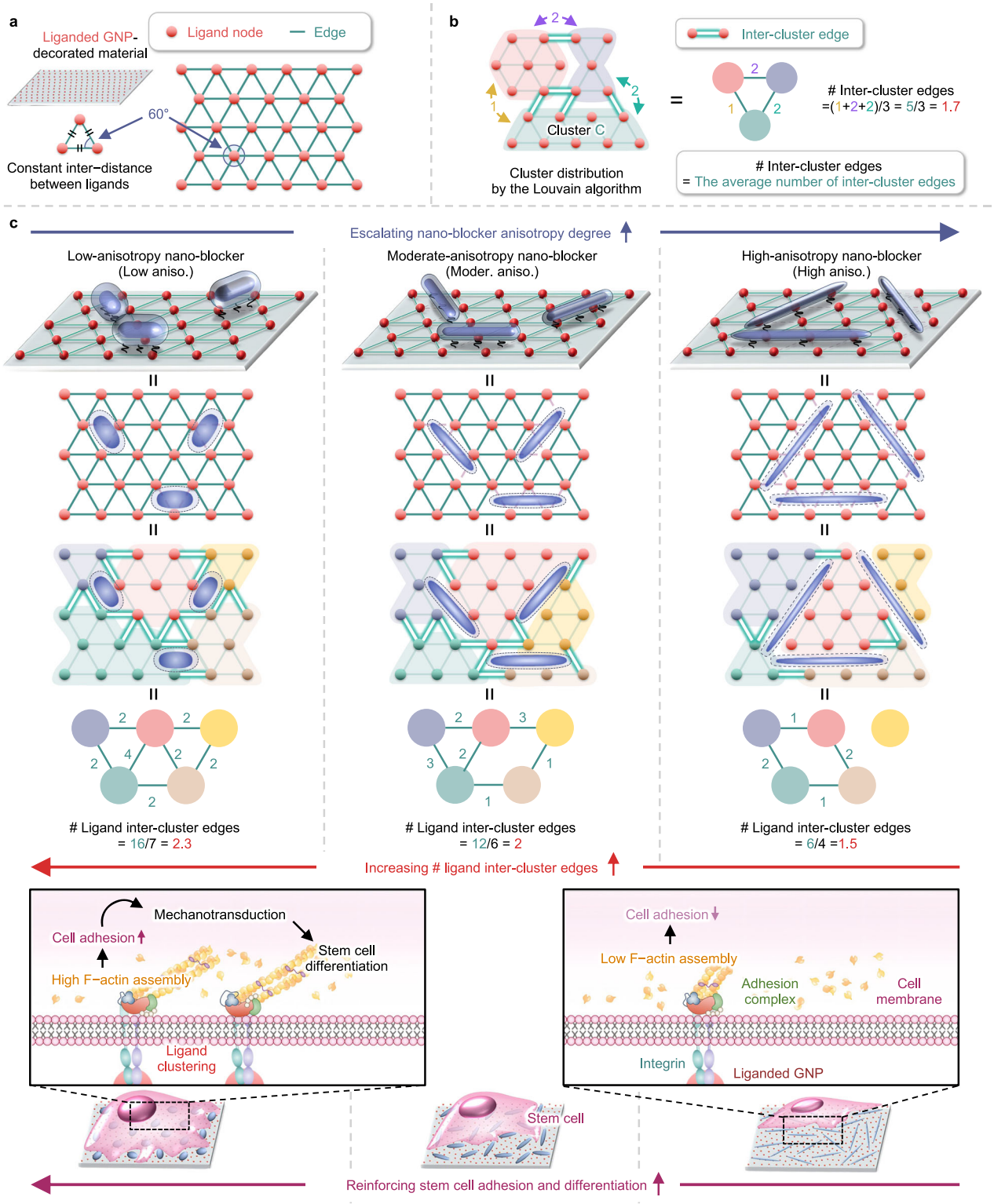

Fig. 1 | Schematic overview of the modeling of interconnected ligand nanocluster for stem cell behavior regulation. a The liganded GNPs on the material surface, which act as ligand nodes constituting interconnected ligands, are homogeneously arranged with equal inter-distances. Due to equal inter-distances, ligand nodes are connected in a way to form equilateral triangles, resulting in a ligand network model with the edges. **b** In the graph theory, the network is partitioned into clusters by the Louvain algorithm based on modularity. Intra-cluster edges were marked by thin green lines, and inter-cluster edges were marked by highlighted white lines. The average number of edges between neighboring clusters is referred to as "# inter-cluster edges". **c** The presence of anisotropic ("aniso.") nano-blockers between the ligand nodes obstruct ligand-to-ligand interconnections, thereby reducing the overall # ligand inter-cluster edges. The lowest anisotropy group ("Low aniso.") exhibits the highest # inter-cluster edges, which promotes the focal adhesion and mechanotransduction of stem cells, and thereby their differentiation, both in vitro and in vivo. In contrast, the highest anisotropy group ("High aniso.") exhibits the lowest # inter-cluster edge, which inhibits the adhesion and differentiation of stem cells.

https://doi.org/10.1038/s41467-024-54557-8

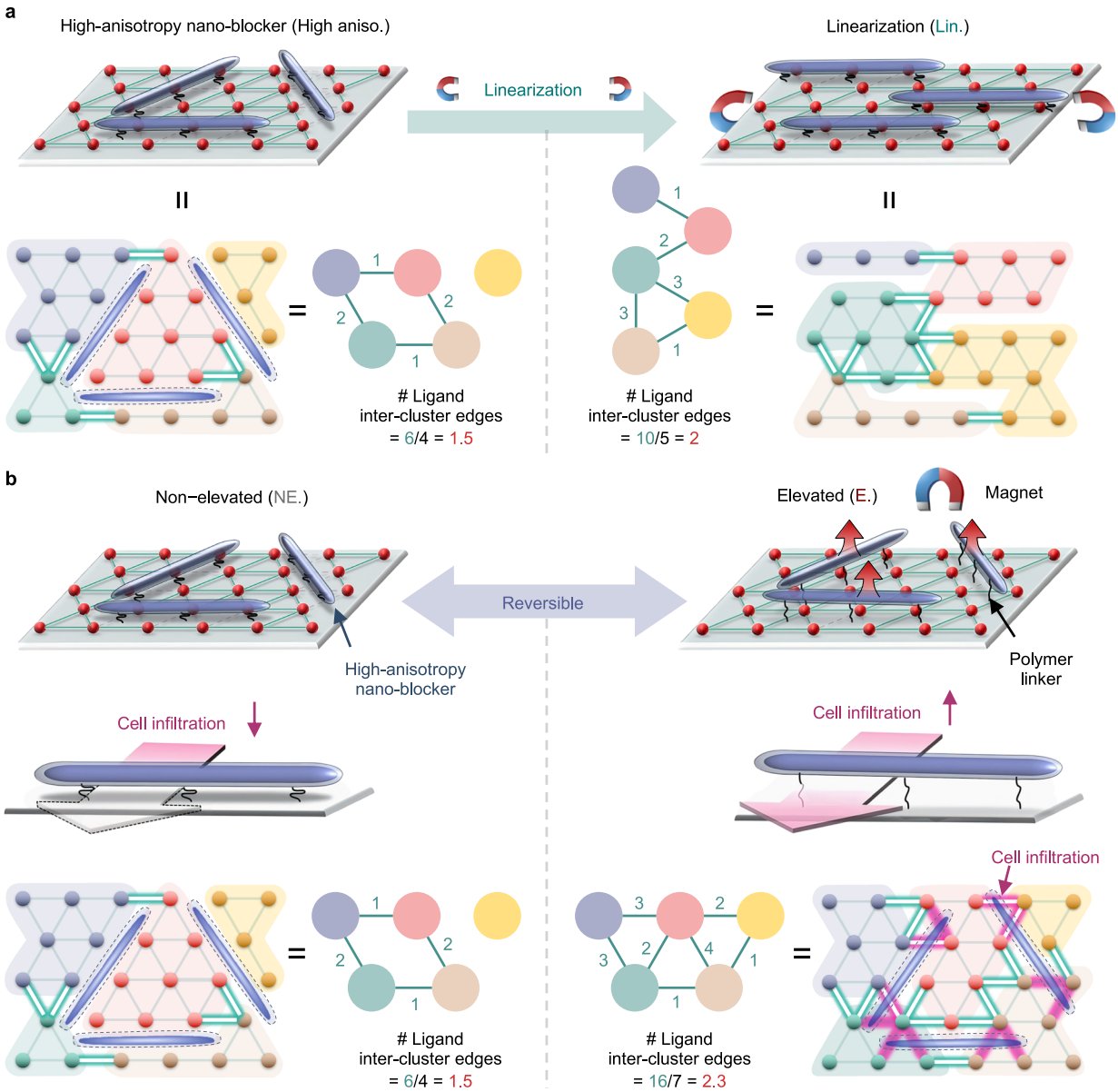

Fig. 2 | Remote control of high-anisotropy nano-blockers for reversible tuning of the average number of ligand inter-cluster edges. Schematic illustrations of remotely controlling high-anisotropy nano-blockers on the interconnected ligand-displaying materials, which reversibly modulates the average number of ligand inter-cluster edges (referred to as "# ligand inter-cluster edges"). **a** Irreversible linearization ("Lin.") of randomly arranged high-anisotropy nano-blockers facilitates local interconnection between the ligand clusters by ordering them, which partly enhances # ligand inter-cluster edges. **b** The ligand nodes are initially disconnected by the nano-blockers ("NE."), which are reconnected via cyclic reversible elevation ("E.") of anisotropic nano-blockers, thereby escalating # ligand inter-cluster edges. The optimization of minimal polymer linker density used to graft the anisotropic nano-blockers to the material allows the cells to sense the ligands as reconnected under the anisotropic nano-blockers in the elevated state and infiltrate through the nano-gap.

Next, the silica-enveloped nano-blockers were meticulously developed to modulate their anisotropy only while adjusting their projected area to be similar and preserving their structure within the silica envelop during the phase transformation from akaganeite to magnetite phase via the reduction process. Specifically, the addition of tetraethyl orthosilicate (TEOS) eight, four, or one time formed a silica envelope with high, moderate, or low thickness, respectively. Annealing at 340 °C for 2 h at a heating rate of 0.45 °C/s from 25 °C to 340 °C mediated the phase transformation in the nano-blocker precursor via a reduction reaction. The structural examination via in situ TEM, in situ HR-TEM with respective in situ FFT analysis, and in situ SAD pattern imaging confirmed the gradual transformation of the akaganeite phase in the nano-blocker precursor core to the magnetite phase in the nano-blocker core with structural preservation within the silica envelop (Fig. 3a, b). In particular, the in situ HR-TEM imaging revealed that the average d-spacing between the successive lattice planes of 5.4 Å in the akaganeite phase before the annealing was distinctly transformed to 3.1 Å in the magnetite phase after the annealing at 340 °C for 2 h (Fig. 3a). Accordingly, distinctive bright spots indicating the (200) plane of the akaganeite phase before the annealing and (220) plane of the magnetite phase after the annealing at 340 °C for 2 h were observed by in situ FFT analysis (Fig. 3a).

The in situ SAD pattern intensity analysis and the real-time movie of the in situ SAD pattern clearly revealed that the distinctive rings of the (310) plane in the akaganeite phase gradually disappeared at the beginning of the annealing at 340 °C, after which distinctive rings of the (220) plane in the magnetite phase gradually emerged over the course of the annealing at 340 °C for 2 h (Fig. 3b and Supplementary

https://doi.org/10.1038/s41467-024-54557-8

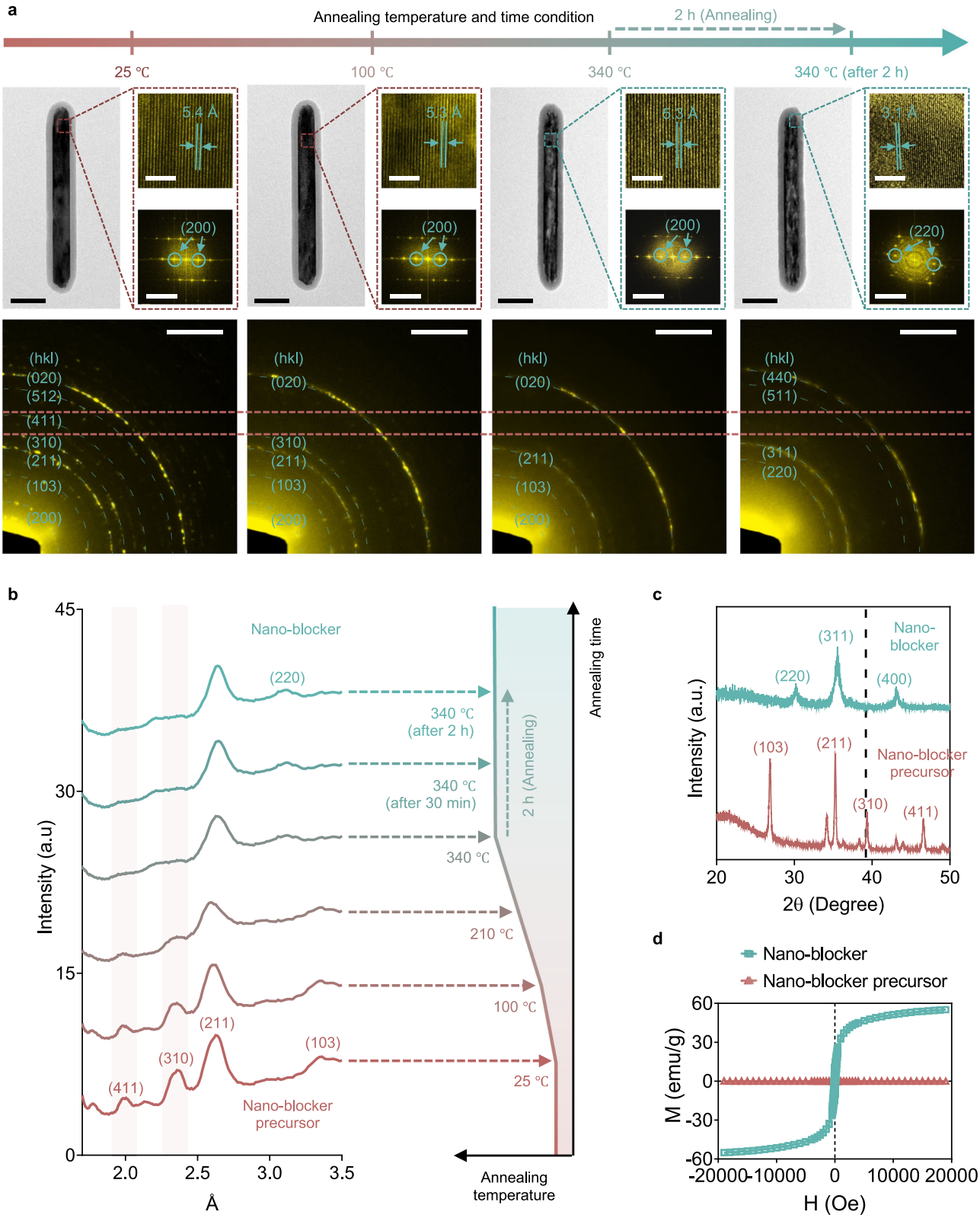

Movie 1). The presence of the magnetite phase was further confirmed via atomic-scale high-resolution scanning TEM (HR-STEM) image of the anisotropic nano-blocker core (magnetite) (Supplementary Fig. 3a). Consistently, X-ray diffraction and vibrating sample magnetometry analyses of the anisotropic nano-blockers and their precursors collectively verified the distinctive crystalline planes of the magnetite phase in the magnetically reversible nano-blockers, which were not present in the akaganeite phase of non-magnetic precursors, further proving their successful phase transformation (Fig. 3c, d).

Interconnected ligand network with tunable nano-blockers

To develop materials displaying reversibly tunable # ligand inter-cluster edges, nano-blockers of each anisotropy (high, moderate, or low) with identical projected areas were grafted to the material surface at identical density via polymer linkers over the interconnected ligand

Fig. 3 | In situ phase transformation enables the formation of reversibly controllable anisotropic nano-blockers. a Schematic illustration of the annealing conditions for the in situ phase transformation in the anisotropic nano-blocker precursor to the anisotropic nano-blocker, along with corresponding in situ transmission electron microscopy (TEM), in situ high-resolution TEM (HR-TEM), in situ FFT, in situ selected area electron diffraction (SAD) pattern images, and **b** in situ SAD pattern intensity analysis. **c** X-ray diffraction (XRD) analysis exhibiting the distinctive crystalline planes and **d** vibrating sample magnetometry (VSM) analysis showing the hysteresis loops of the anisotropic nano-blockers and their precursors after normalization to their respective dry weights. The average d-spacing between the successive lattice planes of the akaganeite phase (5.4 Å) and magnetite phase (3.1 Å) are labeled in the HR-TEM, distinctive bright spots of the akaganeite phase [(200) plane] and the magnetite phase [(220) plane] are labeled in the fast Fourier transform (FFT); distinctive rings corresponding to each akaganeite phase [(103), (211), (310), and (411)] and magnetite phase [(220), (311), (511), and (440)] are labeled in the SAD pattern images. In in situ SAD pattern images in (**a**), red dotted lines were drawn to emphasize the disappearance of (310) and (411) planes of the akaganeite phase after annealing. In in situ SAD pattern analysis in (**b**), rectangular light red boxes were drawn to emphasize the gradual disappearance of (310) and (411) planes of the akaganeite phase after annealing. Distinctive planes of the akaganeite phase [(103), (211), (310), (411), and (521)] and magnetite phase [(220), (311), and (400)] are labeled in the XRD analysis. Scale bars: 100 nm (TEM), 5 nm (HR-TEM), 5 nm^{-1} (FFT), and 2 nm^{-1} (SAD). Source data are provided as a Source Data file.

nodes. This construction enabled the decoupling of other parameters, such as ligand density, when evaluating the effect of only # ligand inter-cluster edges on stem cell behavior decisions. Morphological analysis of the nano-blockers exhibiting low ("Low aniso. nano-blocker"), moderate ("Moder. aniso. nano-blocker"), or high anisotropy ("High aniso. nano-blocker") revealed their significantly different anisotropy [major axis (length) divided by its minor axis (width)] as 2.2 ± 0.4, 5.3 ± 0.3, and 10.4 ± 1.0, respectively, but at nearly identical projected areas of 75.0 ± 2.8 nm^2, 77.0 ± 3.1 nm^2, and 75.1 ± 4.5 nm^2, respectively (Fig. 4a–c and Supplementary Fig. 3b).

TEM, HAADF-STEM, and EDS analyses of the nano-blockers in various anisotropies after phase transformation collectively confirmed the preservation of their rod shape and elements similar to those of their precursors (Fig. 4a and Supplementary Fig. 3c). Furthermore, the line profiles of the EDS images verified the individually optimized dimensions of the core magnetite and silica envelop for each nano-blocker with varying anisotropies (Fig. 4b). Corresponding to the in situ examination, the resultant nano-blockers in various anisotropies all exhibited a magnetite phase-specific crystalline atomic structures and reversible magnetic properties distinct from the non-magnetic akaganeite phase in their precursors, thereby further proving their successful phase transformation regardless of anisotropy (Supplementary Figs. 4 and 5a, b). Each of the low-, moderate-, and high-anisotropy nano-blockers exhibited significantly different lengths and widths of 443.8 ± 53.5 nm and 217.1 ± 26.6 nm, 644.0 ± 20.0 nm and 134.8 ± 11.7 nm, and 920.8 ± 61.6 nm and 91.3 ± 15.8 nm, respectively (Supplementary Fig. 6).

For grafting of the nano-blockers of each anisotropy to the material surface, the anisotropic nano-blockers were amine-functionalized and then coupled with long polymer linkers (molecular weight of 10 kDa) via amide bond formation between *N*-hydroxysuccinimide (NHS) ester in the polymer linkers and the amine group on the nano-blockers (Supplementary Fig. 7). The zeta potential analysis showed a shift in the surface charge from positive to negative values after coupling the polymer linkers to the amine-functionalized nano-blockers in all groups (Supplementary Fig. 8a). The Fourier transform infrared spectra (FTIR) analysis confirmed the emergence of specific amide bonds only after coupling the polymer linkers to the amine-functionalized nano-blockers in all groups consistent with the chemistry of our designed materials (Supplementary Fig. 8b).

To fabricate completely interconnected ligand nodes, gold nanoparticles (GNPs) with a uniform diameter of 20 nm were synthesized, as verified via TEM, HR-TEM, and dynamic light scattering analysis (Supplementary Fig. 9a). Thiolated material surface was homogeneously decorated with the GNPs via gold-thiol bonding[53] that exhibited highly organized arrangement of similar inter-distance of 205.7 ± 16.3 nm between the adjacent GNPs as verified by scanning electron microscopy (SEM) analysis (Supplementary Fig. 9b–d). Such an inter-distance is comparable to the end-to-end distances of fibronectin molecules (about 150 nm) containing RGD ligands in a network of native fibrils in the ECM[54]. The GNP-decorated material was subsequently coated with thiolated RGD tripeptide ligand (CDD RGD) to harness the liganded GNPs as the completely interconnected ligand nodes, followed by grafting of the polymer linker-coupled nano-blockers of varying anisotropies via maleimide-thiol bonding. Due to the negative surface charges of both the liganded GNPs (negative charge of CDD RGD)[55] and the linker-coupled nano-blockers (terminal maleimide group of linkers), electrostatic repulsion occurs thereby positioning the nano-blockers between the liganded GNPs instead of their direct interactions (Supplementary Fig. 8a). Each material exhibited a similar density of liganded GNPs with nearly invariant and retained inter-distances between adjacent liganded GNPs even after the grafting of nano-blockers on the material surface and a similar density of homogeneously grafted nano-blockers in all groups, thus confirming nearly identical ligand density regardless of the anisotropy of the nano-blockers (Fig. 4d, e and Supplementary Figs. 7 and 9c, d). The residual thiolated surface not decorated with the ligand nodes or anisotropic nano-blockers was inactivated by grafting methoxy group-presenting molecules.

Ligand inter-cluster connectivity affects stem cell adhesion

Next, graph theory-based mathematical modeling of interconnected ligand clusters was performed[25,26]. In detail, the liganded GNPs are considered the ligand nodes that constitute interconnected ligands under the nano-blockers that block the ligand-to-ligand edges. To establish the ligand-to-ligand edges between the configured ligand nodes, Delaunay triangulation was employed due to its capability of forming geometrically consistent connections between neighboring ligand nodes (Fig. 1a). This approach ensures that the resulting edges realistically represent the spatial relationship between ligand nodes by maximizing the minimum angle of triangles, thereby promoting uniformity in triangle formation to closely resemble equilateral triangles even in cases where the spacing of gold nanoparticles is not perfectly uniform[56,57]. In this configuration, each group of interconnected ligand nodes was distinguished as a ligand nanocluster by the Louvain algorithm using Python, and the number of edges between neighboring ligand nanoclusters was quantified (Figs. 1b and 5). The number of connected edges between ligand clusters was counted in the SEM images for the nano-blockers of each anisotropy that differentially obstruct connected edges, thereby yielding different average number of inter-cluster edges of the ligand cluster pairs as # ligand inter-cluster edges.

To be specific, the nano-blockers with a higher anisotropy obstructed the interconnected edges between ligand clusters more than the moderate and low anisotropy ones due to their longer length. Hence, # ligand inter-cluster edges escalated with the reduction of nano-blocker anisotropy (Fig. 1b and Fig. 4d, e). Furthermore, linearization of the high-anisotropy nano-blockers by applying a uniform magnetic field "High aniso. (Lin.)" resulted in more locally unobstructed ligand cluster connections by reducing the average inter-angle between the nano-blockers that induces edge disconnection predominantly in one direction. Consequently, inter-cluster connections are retained in multiple directions compared to when the nano-blockers are randomly arranged, thereby escalating # ligand

https://doi.org/10.1038/s41467-024-54557-8

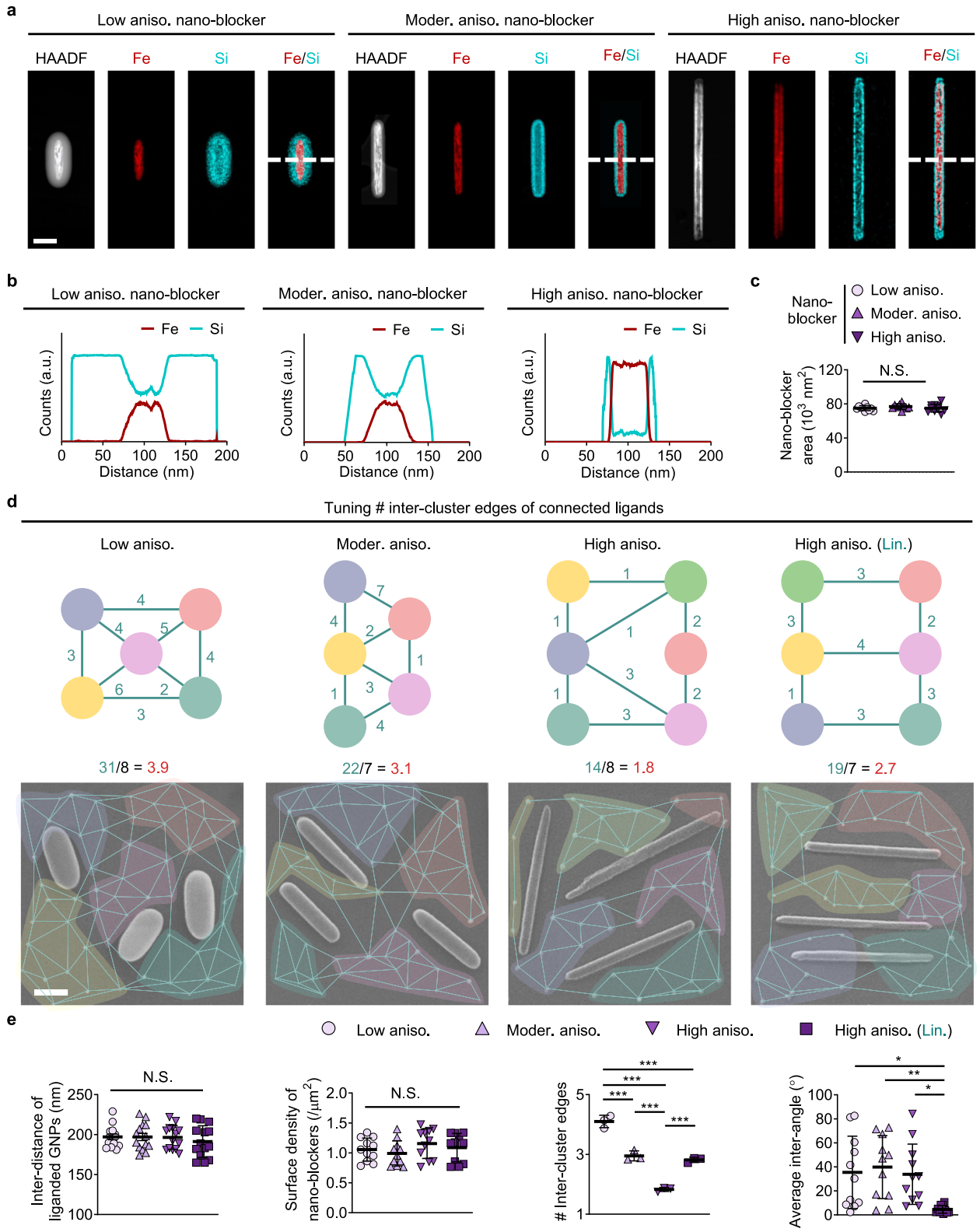

inter-cluster edges over the non-linearized group "High aniso." (Figs. 2a and 4d, e).

We next examined the effect of tuning only # ligand inter-cluster edges of interconnected ligand clusters on stem cell regulation via the anisotropy and linearization of nano-blockers. Due to the relatively large sizes of human mesenchymal stem cells (hMSCs) (hundreds of micrometers of scale), we examined their response to tuning # ligand inter-cluster edges on the microscale. Harnessing materials displaying tuned # ligand inter-cluster edges ["Low aniso.", "Moder. aniso.", "High aniso.", and "High aniso. (Lin)"], stem cells were only added at the beginning of culturing to the material surface of each group, cultured for 48 h, and then fluorescently immunostained. Analysis of the adherent stem cells in each group demonstrated pronouncedly intensified stem cell adhesion with the highest # ligand inter-cluster edges group ("Low aniso.") that exhibited enhanced integrin β1 expression and the highest number of 4′,6-diamidino-2-phenylindole

https://doi.org/10.1038/s41467-024-54557-8

Fig. 4 | Reducing the anisotropy or linearizing the nano-blockers independently escalates # ligand inter-cluster edges. a High-angle annular dark-field scanning transmission electron microscopy (HAADF-STEM) images with elemental energy dispersive spectroscopy (EDS) mapping (Fe from the magnetite phase in the nano-blocker core, and Si from the silica envelop) images marked with white dotted lines at the midsection for **b** the elemental EDS line profiling of the anisotropic nano-blockers ("Low aniso. nano-blocker", "Moder. aniso. nano-blocker", and "High aniso. nano-blocker"). **c** Computation of the projected area of the nano-blocker (10^3 nm^2) ($n = 10$). **d** Scanning electron microscopy (SEM) images of the materials displaying tuned # ligand inter-cluster edges depending on the anisotropy or arrangement of the nano-blockers ["Low aniso.", "Moder. aniso.", "High aniso.", and "High aniso. (Lin.)"] with the representative calculation of # ligand inter-cluster edges. The edges (green lines) within the ligand network formed by nodes in the SEM image were determined by Delaunay triangulation in Python. Each cluster was partitioned using the Louvain algorithm and distinguished by different colors. **e** Corresponding computation of the inter-distance of the liganded GNPs ($n = 10$ edges), the surface density of the anisotropic nano-blockers ($n = 10$ nano-blockers), # ligand inter-cluster edges ($n = 3$ biological replicates; $^{***}p < 0.001$), and the average inter-angle between anisotropic nano-blockers (in absolute value) ($n = 10$ nano-blockers; $^{*}p < 0.05$, $^{**}p < 0.01$). High-anisotropy nano-blockers were linearized on the materials via magnetic annealing during their grafting to the material surface. Scale bars: 200 nm (HAADF-STEM and SEM). Data are shown as the means ± standard errors. Statistical analysis was performed using one-way ANOVA along with the Tukey–Kramer post hoc test. N.S. denotes no statistically significant difference. Source data are provided as a Source Data file.

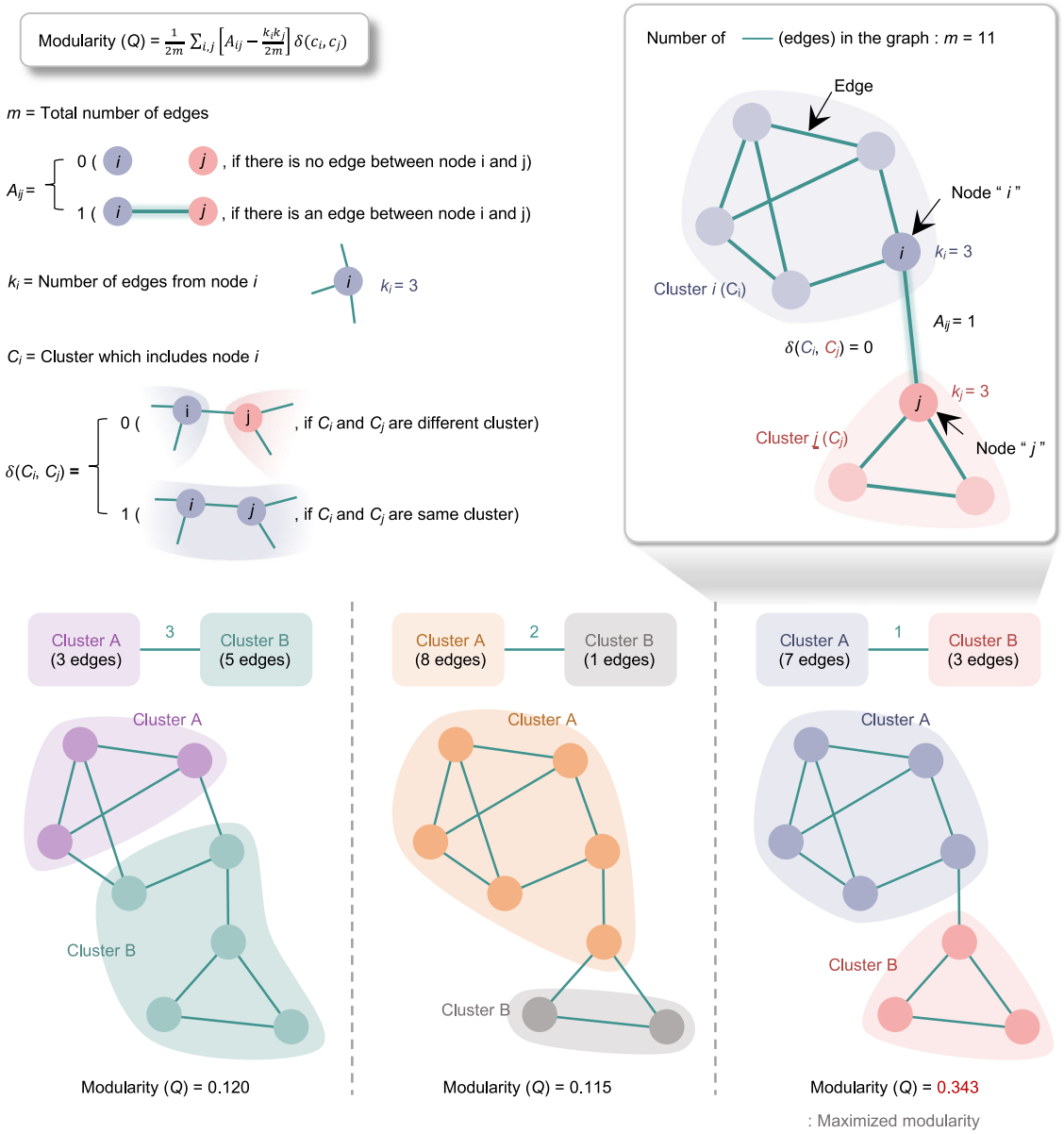

Fig. 5 | Schematic of cluster partition method in the network model by maximizing modularity with the Louvain algorithm. Modularity helps to quantify the interconnectivity of clusters within a network. Factors used in such quantification in the modularity formula include the total number of edges (m), the presence of an edge between the two nodes (A_{ij}), the number of edges from each node (k_i or k_j), and the cluster coincidence of node pair [$\delta(C_i, C_j)$]. The modularity is maximized in the optimal cluster partition where the number of intra-cluster (within the cluster) edges is maximized while the number of inter-cluster (between the clusters) edges is minimized. The optimized cluster partition of a given network can be found using the Louvain algorithm in Python, where this formula is included.

(DAPI)-positive cells as well as the highest focal adhesion number and the largest actin-positive area in each cell with the lowest cell aspect ratio compared with the lowest # ligand inter-cluster edges group ("High aniso.") (Supplementary Figs. 10a, b and 11a, b). Interestingly, the adhesion of stem cells that was promoted the least on the "High aniso." group exhibiting the lowest # ligand inter-cluster edges with the non-ordered nano-blockers was partly enhanced via nano-blocker linearization ["High aniso. (Lin.)"] that escalated # ligand inter-cluster edges by the ordered nano-blockers (Supplementary Figs. 10a, b and 11a, b).

Focal adhesion through mechanosensitive proteins, such as paxillin, induces tension from stress fibers, which promotes the translocation of mechanotransduction regulator yes-associated protein (YAP), thereby regulating the differentiation of stem cells[58,59]. Furthermore, the corresponding trend was revealed in the analysis of following stem cell mechanotransduction and differentiation by either culturing for 48 h in growth medium or 72 h in osteogenic differentiation medium, in which the stem cells showed higher translocation of YAP (mechanotransducer) and RUNX2 (early osteogenic differentiation marker) to the nucleus at a level proportional to # ligand inter-cluster edges (Supplementary Fig. 12a, b). Taken together, these results suggest that the escalation in # ligand inter-cluster edges, whether it was achieved through a reduction in anisotropy or linearization of nano-blockers, proportionately facilitates the adhesion, mechanosensing, and differentiation of stem cells.

A series of control experiments were conducted to verify whether such regulation of stem cells is indeed a # ligand inter-cluster edges-tuning-specific effect. First, stem cell adhesion was only highly supported when the interconnected GNPs were coated with ligands in the absence of nano-blockers, thereby proving the necessity of the ligands for stem cell regulation (Supplementary Fig. 13a, b). It has recently been reported that the membrane bending energy of cells hinders their adhesion, including focal adhesion of stem cells, to highly curved surfaces[60–63]. In the present study, high-anisotropy nano-blockers of lower diameter exhibited higher curvature due to the inversely proportional relationship between the curvature and diameter of the nano-blockers. Thus, the high-anisotropy nano-blockers exhibiting higher curvature would require cell membranes to bend slightly more when adhering to the material surface and thus not readily adhere as opposed to the low-anisotropy nano-blockers exhibiting lower curvature. This effect of curvature may have contributed to weaker stem cell adhesion in the high-anisotropy nano-blockers in addition to the effect of # ligand inter-cluster edges (Supplementary Figs. 10a, b and 11a, b). However, tuning the anisotropy (and thus the curvature) of nano-blockers in the conditions free of the ligand resulted in similar levels of stem cell adhesion in all groups, thereby indicating that the effect of membrane curvature alone is not significant (Supplementary Fig. 14a, b). Meanwhile, the linearization of the low- and moderate-anisotropy nano-blockers ["Low aniso. (Lin.)" and "Moder. aniso. (Lin.)"] only slightly promoted stem cell adhesion compared with their respective randomly oriented states ("Low aniso." and "Moder. aniso.") (Supplementary Fig. 15a, b). Such insignificant cell-regulatory effect of linearizing nano-blockers in lower-anisotropy groups could be attributable to that they do not effectively obstruct the ligand-to-ligand interconnections even in their random orientation.

Cyclic nano-blocker elevation regulates stem cell adhesion

Since tuning # ligand inter-cluster edges by linearizing the nano-blockers of high-anisotropy was proved to be the most efficient method for stem cell regulation, we used this approach for the examination of remote and reversible elevation-mediated stem cell regulation. To this end, a piece of permanent magnet (295 mT) was either employed or non-employed above the materials to mediate the reversible elevation (E.) or non-elevation (NE.) of the high-anisotropy nano-blockers, respectively (Fig. 6a). In the linear height profile, the nano-blocker was found to be surrounded by the liganded GNP nodes (Supplementary Fig. 16). In the TEM images, the nano-blocker showed the diameter of approximately 91.3 nm and the GNPs demonstrated the diameter of approximately 20.0 nm, both of which dimensions were consistent in the atomic force microscopy (AFM) images (Supplementary Figs. 6 and 9a). The computation of peak heights of the reversibly elevated nano-blockers over two cycles (NE.-E.-NE.-E.-NE.) using in situ AFM images showed the measured heights of 140.0 ± 0.7, 155.3 ± 0.8, 140.5 ± 0.9, 155.5 ± 1.0, and 140.5 ± 0.9 nm, respectively. Thus, the average peak height of the nano-blocker was 140.3 ± 0.9 nm in the NE. state, and 155.4 ± 0.9 nm in the E. state (Fig. 6b, c and Supplementary Fig. 16).

We next hypothesized that when the nano-blockers are elevated, a low density of the polymer linkers coupled to the nano-blockers would enable cell infiltration to access the ligand nodes through nano-gaps, which would be blocked in the case with a high density of polymer linkers. To prove this hypothesis, Ellman's assay was performed to compute the concentration of L-cysteine that reacted with the polymer linker-coupled nano-blockers via thiol-ene bonds when a low or high density of polymer linkers was used (Fig.6e). A low or high molarity of reacted L-cysteine signified a low or high density of polymer linkers coupled to the nano-blockers, respectively (Fig. 6d, e). Indeed, this was consistent with the low peak of the amide bond observed in the FTIR analysis signifying the low density of polymer linkers coupled to the nano-blockers (Supplementary Fig. 8b).

For the verification of such a hypothesis by visualizing integrins recruited to the interconnected ligands under the tuning of # ligand inter-cluster edges, immuno-GNP (IGNP) tagging of integrin β1 in stem cells was conducted using larger GNPs (40 nm in diameter) so that they were discernible from the smaller GNPs (20 nm in diameter) employed as ligand nodes (Supplementary Fig. 17a–d). The IGNP (white) tagging of integrin of stem cells (green) was employed after 48 h of culturing on the materials displaying reversibly tunable # ligand inter-cluster edges. Moreover, its overlay with EDS mapping verified the presence of the nano-blockers under the cells by identifying the Fe element in the nano-blocker core (Fig. 6f). Following images of the IGNP-tagged stem cells confirmed facilitated cell infiltration through the nano-gaps under the elevated high-anisotropy nano-blockers when using a low linker density (used in the present study) as compared with hindered cell infiltration under them when using a high linker density (Fig. 6g). This observation clearly indicates that the optimized low linker density enabled cells to sense the ligand nodes as interconnected under the elevated nano-blockers, thereby escalating the overall # ligand inter-cluster edges (Fig. 2b). Moreover, a higher number of integrin-tagged IGNPs, signifying facilitated integrin recruitment, was found around the ligand nodes with escalating # ligand inter-cluster edges (Fig. 5h). Compared analysis of the inter-distance of liganded GNPs before and after cell culturing revealed their constant density, thereby proving the stability of the ligand nodes on the materials for the application of mathematical modeling (Figs. 4e and 6h).

However, the elevation of the nano-blockers exhibiting lower anisotropy ["Low aniso. (E.)" and "Moder. aniso. (E.)"] for the tuning of # ligand inter-cluster edges was not as efficient at intensifying stem cell adhesion. This could be attributed to them already showing a high # ligand inter-cluster edges in the non-elevated state, which could not be further escalated in the elevated state (Supplementary Fig. 18a, b).

Subtraction of the diameter of high-anisotropy nano-blockers (approximately 91.3 nm) from their average peak height in "E." state and "NE." state resulted in nano-gaps of 64.1 nm and 49.0 nm, respectively, below the elevated nano-blockers. Given that we used a long polymer linker with a molecular weight of 10 kDa, its lengths of 49.0 nm and 64.1 nm in the non-stretched and stretched states, respectively, are consistent with previously reported analyses[64,65]. Thus a small height disparity of only approximately 15.1 nm via the reversible dynamic control of nano-blocker elevation effectively modulated the

https://doi.org/10.1038/s41467-024-54557-8

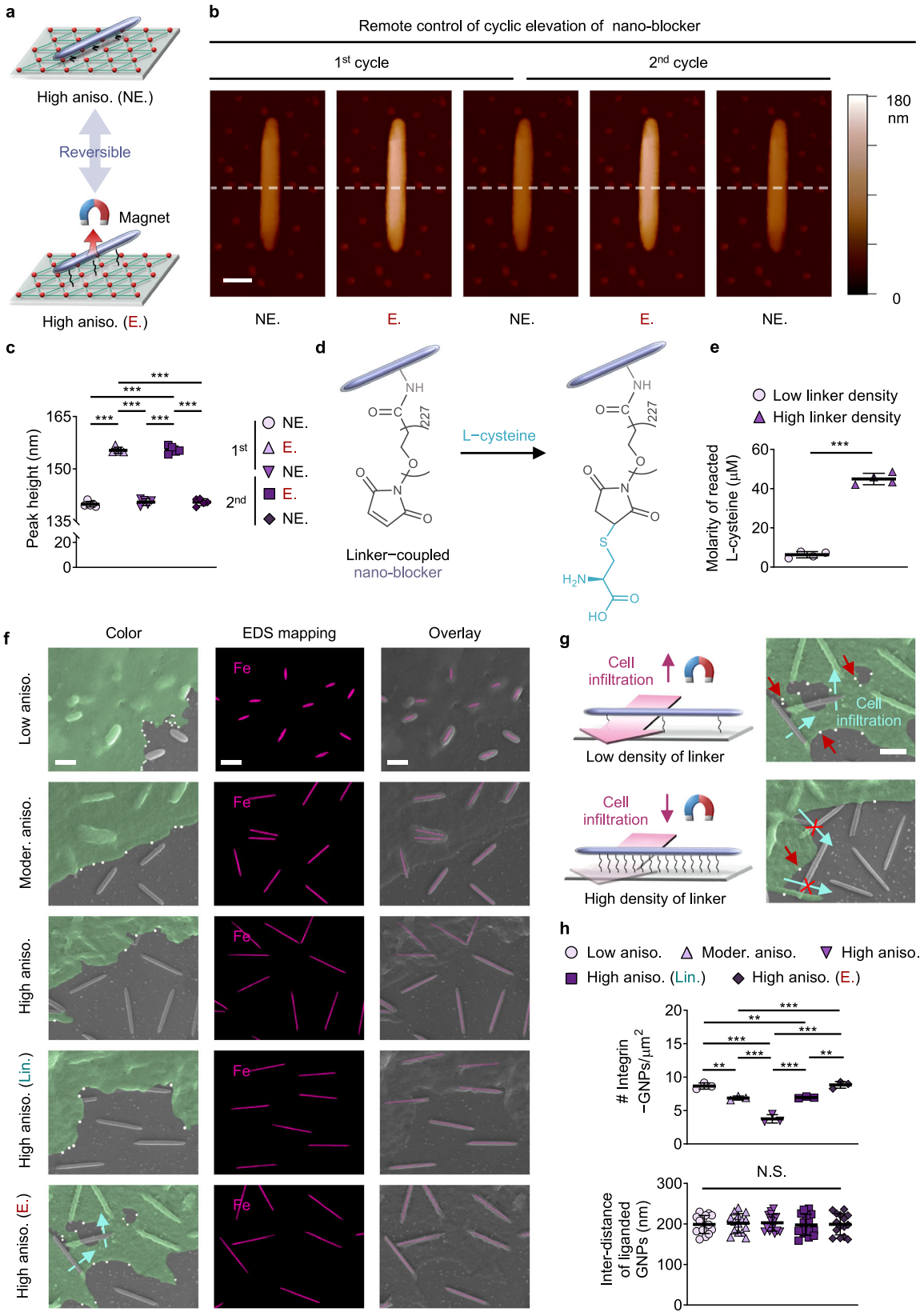

infiltration of stem cells. This rather striking phenomenon could be regulated by cellular filopodia (dynamic slim extensions of cytoplasmic protrusions from the cell membrane) that can sense ligands via integrin receptors (around 10 nm in size) present at the cell membrane, thereby facilitating cellular adhesion and spreading[33,58,59]. Filopodia typically exhibits a diameter slightly above 60 nm, and can therefore slide through the nano-gaps with a height of 64.1 nm under the elevated nano-blockers[66]. The height of this nano-gap lies just above the threshold size of filopodia that enables it to access the ligand nodes under the nano-blockers, thereby regarding the ligand nodes interconnected across the nano-blockers. Since the filopodia form focal adhesions with the adhered materials, a significantly higher focal

Fig. 6 | Cyclic elevation of anisotropic nano-blockers escalates # ligand inter-cluster edges that reversibly stimulate integrin recruitment. a Schematic illustration of the cyclic elevation ("E.") and non-elevation ("NE.") of high-anisotropy nano-blockers grafted to the materials ("High aniso.") that can reversibly escalate # ligand inter-cluster edges. **b** In situ atomic force microscopy (AFM) images of the cyclic elevation of high-anisotropy nano-blockers for reversible tuning of # ligand inter-cluster edges repeated over two cycles marked with white dotted lines at the midsection for height analysis and **c** the subsequent computation of peak height changes of the nano-blockers ($n = 5$; $^{***}p < 0.001$). **d** Schematic illustration of utilizing L-cysteine to compute the number of polymer linkers coupled to the nano-blocker surfaces using Ellman's assay for (**e**) computation of the reacted L-cysteine molarity on the anisotropic nano-blockers either coupled with a low (used in this study) or high density of polymer linker ($n = 4$; $^{***}p < 0.001$). **f** Scanning electron microscopy (SEM), elemental energy dispersive spectroscopy (EDS) mapping (Fe from the magnetite phase of the nano-blocker core), and overlay images of immuno-GNP (IGNP)-based tagging of integrin in stem cells adhered to the materials displaying tunable # ligand inter-cluster edges. **g** Schematic illustration and SEM images of the IGNP-tagged integrin in stem cells that could infiltrate through nano-gaps (at low polymer linker density showing the image in Fig. 5f) or were blocked (at high polymer linker density) when the anisotropic nano-blockers were elevated. **h** Computation of the average number of IGNP-tagged integrin in stem cells at the cell boundary per unit area (μm^2) ($n = 3$ gold nanoparticles; $^{**}p < 0.01$; $^{***}p < 0.001$) and inter-distance of the liganded GNPs after cell culturing ($n = 10$ edges). A piece of permanent magnet (295 mT) was employed ("E.") or non-employment ("NE.") above the materials for the cyclic elevation of high-anisotropy nano-blockers. High-anisotropy nano-blockers were linearized ("Lin.") on the materials via magnetic annealing during their grafting to the material surface. In the SEM images, stem cells and IGNPs are each colored green and white, respectively. Scale bars: 200 nm (AFM) and 500 nm (SEM and EDS). Data are shown as the means ± standard errors. Statistical analysis was performed using one-way ANOVA along with the Tukey–Kramer post hoc test. N.S. denotes no statistically significant difference. Source data are provided as a Source Data file.

adhesion number in the "E." state compared with the "NE." state offers further evidence for filopodia being able to reach the highly interconnected ligand nodes under the nano-blockers were in the elevated state[59]. In stark contrast, filopodia could not slide through the nano-gaps with a height of 49.0 nm when the nano-blockers were in the non-elevated state, thereby suppressing them from reaching the ligand nodes disconnected across the nano-blockers.

Our present report of employing 1-D anisotropic-shaped magnetic nano-blockers to reversibly regulate # ligand inter-cluster edges is distinctly different from previous reports that showed the modulation of cell behaviors via 1-D micro/nanostructures[32,36,51,52,67], or clustering[31] since they did not modulate the blocking of the ligands to regulate ligand interconnectivity with systematic modeling. Taken together, our findings prove that cyclic elevation of anisotropic nano-blockers can remotely manipulate # ligand inter-cluster edges to facilitate reversible integrin recruitment-mediated stem cell adhesion, which can be unraveled through systematic modeling of ECM interconnectivity.

Cyclic tuning of ligand network reverses stem cell behaviors

Filopodia formation can drive focal adhesion, which facilitates cellular mechanotransduction and differentiation[58,59]. Therefore, we next examined whether cyclic tuning of # ligand inter-cluster edges can modulate the focal adhesion of stem cells to reversibly regulate the mechanotransduction that leads to the differentiation of stem cells. To this end, stem cells were cultured either in a growth medium to instigate focal adhesion and mechanosensing or osteogenic differentiation medium to instigate differentiation. The employment and non-employment of a piece of permanent magnet (295 mT) above the materials were either switched or maintained every 24 h up to 72 h ("NE.-NE.-NE.", "NE.-E.-NE.", "E.-NE.-E.", and "E.-E.-E.") for cyclic tuning of # ligand inter-cluster edges. The immunostained fluorescent imaging and analysis showed that stem cells examined right after being cultured with nano-blockers in the elevated state consistently exhibited a significantly escalated number of DAPI-positive cells, focal adhesion number of each cell, actin-positive area of each cell, and nuclear/cytoplasmic intensity ratios of YAP and RUNX2 expression, along with a lower cell aspect ratio (Fig. 7a, b and Supplementary Figs. 19 and 20a, b). This indicates that the adhesion, mechanotransduction, and differentiation of stem cells could only be reversibly promoted after elevating the nano-blockers. On the contrary, stem cells examined right after being cultured with nano-blockers in the non-elevated state consistently exhibited the opposite trend. The quantitative examination of stem cell differentiation via western blotting analysis further corroborated this result, in which stem cells cultured on cyclically controlled groups whose culturing ended with the nano-blockers in the elevated state ("E.-NE.-E.", and "E.-E.-E.") exhibited higher expression of both RUNX2 and ALP (osteogenic differentiation marker) proteins (Fig. 7b and Supplementary Fig. 21). These results suggest that stem cells can sense and respond to the reversible escalation of # ligand inter-cluster edges via cyclic elevation of the nano-blockers, resulting in their mechanosensing and differentiation being regulated accordingly.

The activation of Rho signaling mediates actin polymerization, thereby supporting the formation of filopodia, which drives the mechanosensing and differentiation[58,59]. Therefore, to assess molecular signaling that governs # ligand inter-cluster edges-mediated regulation of stem cell mechanosensing and differentiation, adhesion-related proteins and their inhibition were investigated. While remotely tuning # ligand inter-cluster edges, stem cells were cultured for 48 h on the materials displaying remotely tuned # ligand inter-cluster edges in growth medium or 72 h in osteogenic differentiation medium, both of which were supplemented with one of the following cell adhesion-related pharmacological inhibitors of myosin II by ML9, actin polymerization by Swinholide A, or rho-associated protein kinase (ROCK) by Y27632. Although the expressions of both YAP and RUNX2 were stimulated in correspondence with escalating # ligand inter-cluster edges free of any inhibitor, suppressing any of the adhesion-related molecular mechanisms by each inhibitor's nullified # ligand inter-cluster edges-mediated stem cell-regulatory effect (Fig. 8a, b). Taken together, these analyses unravel the regulatory mechanisms of stem cell behaviors via the tuning of # ligand inter-cluster edges that involve myosin II, actin polymerization, and ROCK signaling.

Ligand inter-cluster connectivity governs stem cell in vivo

The network interconnectivity of natural ECM incessantly varies over time which determines its dynamic function to modulate the filopodia formation in stem cells that regulates their mechanotransduction and differentiation in vivo[1,58,59,68]. Thus, the applicability of modeling of ECM-mimetic tunable # ligand inter-cluster edges in vivo was preliminarily examined to unravel the regulation of stem cell behaviors that can support neo-tissue formation. As a proof-of-concept, materials displaying reversibly tunable # ligand inter-cluster edges were implanted in the subcutaneous pockets of mice, after which hMSCs were injected thereon (Fig. 9a). The mice were kept anesthetized to immobilize them to ensure stable adhesion of the stem cells to the materials without any breakage and stem cell leakage. Furthermore, a piece of permanent magnet was coupled to the backs of the mice to mediate the elevation of high-anisotropy nano-blockers that escalate # ligand inter-cluster edges. The coupling and uncoupling of the magnet were either switched or maintained every 3 h for 6 h ("NE.-NE.", "NE.-E.", "E.-NE.", and "E.-E.") for time-resolved tuning of # ligand inter-cluster edges.

Immunostained fluorescent imaging and quantitative analysis of co-localization of the human-specific HuNu and DAPI confirmed that the adherent cells were then injected hMSCs. The examination of their trends corroborated with the in vitro results, where not only the

https://doi.org/10.1038/s41467-024-54557-8

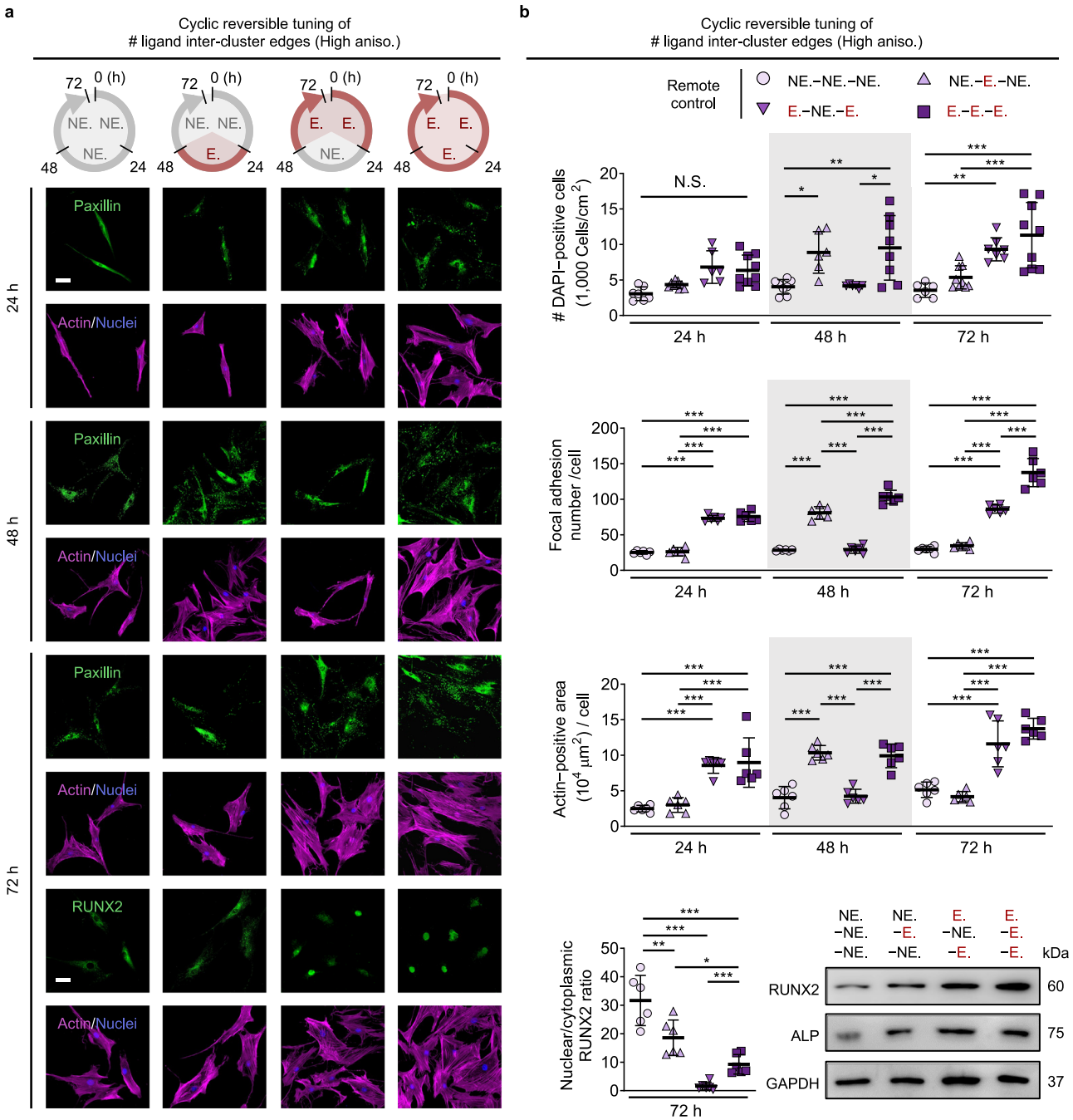

Fig. 7 | Remote cyclic tuning of # ligand inter-cluster edges reversibly regulates stem cell behaviors. a Immunostained fluorescent images of paxillin co-stained with F-actin and nuclei (DAPI) of adherent stem cells after 24 h, 48 h, or 72 h of culturing in growth medium and RUNX2 co-stained with F-actin and nuclei after 72 h of culturing in differentiation medium on materials displaying a cyclically tunable # ligand inter-cluster edges. **b** Computation of the DAPI-positive cell density ($n = 6$–9 biological replicates; $^{*}p < 0.05$; $^{**}p < 0.01$; $^{***}p < 0.001$), focal adhesion number ($n = 6$ cells; $^{***}p < 0.001$), actin-positive cell area ($n = 6$ cells; $^{***}p < 0.001$), and nuclear/cytoplasmic intensity ratio of RUNX2 ($n = 6$ cells; $^{*}p < 0.05$; $^{**}p < 0.01$; $^{***}p < 0.001$) along with western-blot analysis of RUNX2 and ALP protein expression (normalized to GAPDH) of adherent stem cells. The employment and non-employment of a piece of permanent magnet (295 mT) above the materials were either switched or maintained every 24 h for up to 72 h ("NE.-NE.-NE.", "NE.-E.-NE.", "E.-NE.-E.", and "E.-E.-E."). Scale bars: 50 μm (confocal microscopy). Data are shown as the means ± standard errors. Statistical analysis was performed using one-way ANOVA along with the Tukey–Kramer post hoc test. N.S. denotes no statistically significant difference. Source data are provided as a Source Data file.

number of HuNu-positive cells but also the focal adhesion number, actin-positive area, and nuclear/cytoplasmic intensity ratios of YAP and RUNX2 were escalated while the cell aspect ratio was reduced for stem cells subjected to time-resolved ligand degree tuning that ended in the elevated state of nano-blockers ("NE.-E." and "E.-E.") (Fig. 9b, c and Supplementary Fig. 22). Furthermore, the implanted materials subjected to remote tuning remained stable in the in vivo microenvironment for 24 h and exhibited similar density of both the GNPs and nano-blockers before and after implantation (Supplementary Fig. 23a, b). They were non-cytotoxic as evaluated locally (subcutaneous tissue) and systemically (liver, heart, spleen, and kidney) by the preservation of cellular organization after implantation in the mice, suggesting their safe applicability (Fig. 9d). This is consistent with prior findings of applying a magnetic field to manipulate nanomaterials

https://doi.org/10.1038/s41467-024-54557-8

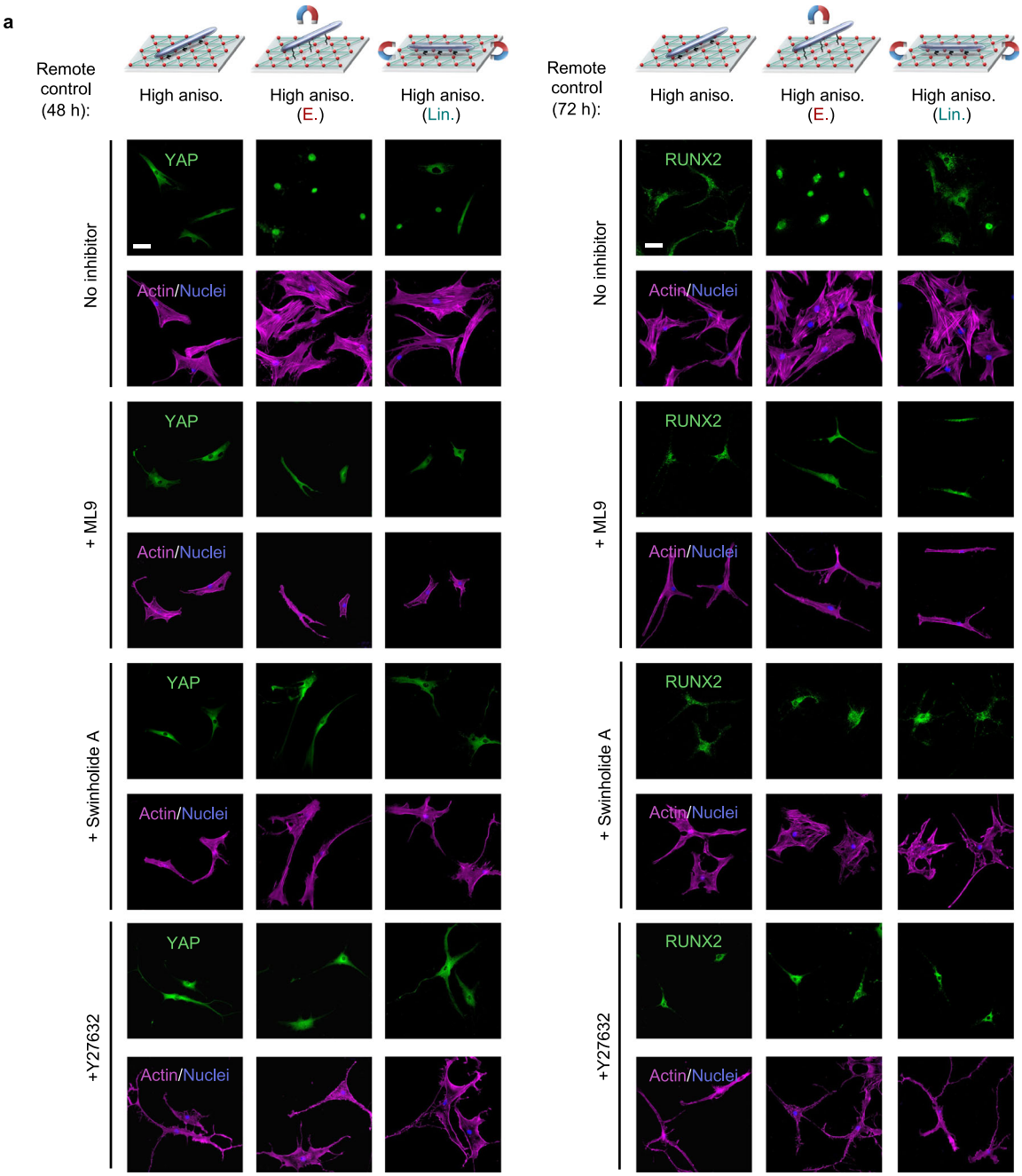

remaining non-toxic[48,69]. Altogether, these results cooperatively propose that tuning the mathematically modeled # ligand inter-cluster edges in vivo could safely and efficiently regulate the mechanosensing-mediated stem cell behaviors, thereby presenting promising applicability for systemically unraveling their tissue-regenerative therapeutic effect.

Discussion

We introduced the concept of utilizing the graph theory to mathematically model # inter-cluster edges of interconnected ligand GNP nodes by varying the anisotropy of homogeneously arranged nanoblockers with identical projected areas and surface density, enabling independent tuning of # ligand inter-cluster edges. Increasing the

Fig. 8 | Dynamic stem cell behaviors regulated by remote tuning of # ligand inter-cluster edges is driven by the adhesion-relevant molecular machinery. **a** Immunostained fluorescent images of YAP co-stained with F-actin and nuclei of adherent stem cells after 48 h of culturing in stem cell growth medium or RUNX2 co-stained with F-actin and nuclei after 72 h of culturing in stem cell differentiation medium on materials displaying remotely tunable # ligand inter-cluster edges. In each case, the medium was supplemented with ML9 (a myosin II-inhibitor), Swinholide A (Swinh. A; an actin polymerization-inhibitor), or Y27632 (a ROCK-inhibitor) or without any of the inhibitors (the control). **b** Computation of nuclear/cytoplasmic intensity ratio of YAP ($n = 6$ cells; $^{***}p < 0.001$) and RUNX2 ($n = 6$ cells; $^{*}p < 0.05$; $^{***}p < 0.001$) expression in adherent stem cells. Scale bar: 50 μm (confocal microscopy). Data are shown as the means ± standard errors. Statistical analysis was performed using one-way ANOVA along with the Tukey–Kramer post hoc test. N.S. denotes no statistically significant difference. Source data are provided as a Source Data file.

anisotropy of the magnetic nano-blockers flexibly grafted to the material surface proportionally blocked ligand-to-ligand interconnection between neighboring ligand clusters that decreased # ligand inter-cluster edges and thus deactivated stem cells.

We also present two approaches to remotely enhancing # ligand inter-cluster edges. First, magnetically linearizing the nano-blockers directionally increased the number of ligand interconnections, which thus escalated # ligand inter-cluster edges. Second, cyclic remote control of magnetically elevating the nano-blockers provided nanogaps through which integrin-presenting filopodia of stem cells could infiltrate and contact the interconnected ligand nodes thereunder, thereby strengthening their focal adhesion, mechanosensing, and resulting differentiation, both in vitro and in vivo. Yet, it is acknowledged the limitations of our preliminary animal experiments in fully capturing the behaviors of cells interfacing with the materials. While we are committed to extending our mathematical modeling concepts to more complex and sophisticated three-dimensional environments in the future, such an expansion would be overly complicated for the current work.

In summary, the remodeling of natural ECM reversibly modulates the connection and disconnection in the liganded network structure that governs its function, physiology, pathology, and disease development. Therefore, designing such diverse ECM-mimetic materials and systematically elucidating the effect of regulating material interconnectivity on various cell behaviors, such as the differentiation of stem cells into different lineages[70,71] or the adhesion and invasion of tumor cells[72], via mathematical modeling, can broaden the horizons of biomaterial applications of these materials. With further development of computational modeling and machine learning[73,74], our approach can be potentially applied to analyzing essentially any other ECM-emulating functional geometries[58] by designing the structures of remotely regulatable nano-blockers to precisely and reversibly regulate and elucidate cell-material interactions for advancing regenerative therapies.

Methods

Ethics declaration

All mouse experiments were performed after obtaining approval from the Institutional Animal Care and Use Committee of Korea University (KOREA-2021-0006). The mice were housed in a standardized environment with a 12 h light/12 h dark cycle at 18–25 °C under 50 ± 5% relative humidity in a semi-specific pathogen-free (SPF) environment at Laboratory Animal Research Center of Korea University College of Medicine. The animals were monitored daily for any clinical symptoms (e.g., re-epithelialization, weight loss, inflammation, infection, bleeding). After each experiment, mice were euthanized via CO_2 asphyxiation in a sealed chamber, with CO_2 gas concentration gradually increased at a rate of 10–30% per minute and maintained for at least 5 min. After respiration ceased, the animals were checked for heartbeat cessation to confirm complete euthanasia.

Tuning only the anisotropy of silica-enveloped nano-blocker precursors irrespective of the projected area

For the meticulous tuning of the anisotropy degree (i.e., low, moderate, and high) of remotely manipulable nanorods (nano-blockers), precursor nanorods in akaganeite phase (β-ferric oxyhydroxide) prior to the formation of silica envelop were first synthesized in different dimensions. Their nanorod structures were achieved through the hydrolysis process of iron(III) chloride ($FeCl_3$), resulting in the preferential growth of the akaganeite phase (monoclinic structure) in the [010] direction. The growth rate of the akaganeite nanorods is directly proportional to the $FeCl_3$ concentration, in which their higher concentration results in the nanorods with higher anisotropies. Hence, the akaganeite nanorods with varied anisotropies were synthesized through a sequential procedure. First, controlled amounts (2.5 g, 5.0 g, or 7.5 g) of $FeCl_3 \cdot 6H_2O$ were dissolved in deionized (DI) water and left at 85 °C overnight, resulting in the akaganeite nanorods with low, moderate, and high anisotropies, respectively. They were then isolated by washing with centrifugation using ethanol and then suspended in 10 mL of DI water. Finally, the precursor akaganeite nanorods in various anisotropies prior to the formation of silica envelop were stabilized in 90 mL of DI water containing 2 wt% polyvinylpyrrolidone (PVP, molecular weight of 10 kDa) overnight, washed with centrifugation using DI water, and finally suspended in 12 mL of DI water.

For the adjustment of their projected area to be similar and their structural preservation during the phase transformation from akaganeite to magnetite phase (via reduction), a silica envelope was formed on the surfaces of each precursor akageneite nanorods of different anisotropies. The thickness of silica envelops on each akaganeite nanorod differed depending on the desired anisotropy. To this end, 5 mL of DI water containing 1.25 mL of ammonium hydroxide was added to 1 mL of stabilized akaganeite nanorods in 25 mL of ethanol, followed by stirring for 20 min. The number of times TEOS was added to the mixture was controlled depending on the desired anisotropies (low, moderate, and high) of the silica-enveloped nanorods. For the low or moderate anisotropy of the nanorod structure of akageneite enveloped by silica (nano-blocker precursors) ("Low aniso. nano-blocker precursor" and "Moder. aniso. nano-blocker precursor"), 12.5 μL of TEOS was added eight or four times with 15-min interval between each addition to the akaganeite nanorods with low or moderate anisotropies, respectively. For high-anisotropy nano-blocker precursors ("High aniso. nano-blocker precursor"), 10 μL of TEOS was added once to the akaganeite nanorods with high anisotropy. In each case, the mixture was then stirred at room temperature for 2 h, washed with centrifugation using ethanol, and suspended in 3 mL of DI water.

In situ phase transformation for converting anisotropic nano-blocker precursors to anisotropic nano-blockers

The annealing-mediated reduction was applied to mediate in situ phase transformation of the akaganeite phase in the anisotropic nano-blocker precursors into the magnetite phase to produce the nanorod structure of magnetite enveloped by silica envelope (nano-blocker) that is remotely and reversibly manipulable. To this end, 1.5 mL of nano-blocker precursors in various anisotropies were each mixed with 10 mL of triethylene glycol (TEG) and heated at 340 °C for 2 h under a nitrogen atmosphere. After the treatment via in situ phase transformation, the resulting anisotropic nano-blockers were washed with centrifugation using ethanol and suspended in 6 mL of ethanol. Each "Low aniso. nano-blocker precursor", "Moder. aniso. nano-blocker precursor", and "High aniso. nano-blocker precursor" transformed into "Low aniso. nano-blocker", "Moder. aniso. nano-blocker", and "High aniso. nano-blocker", respectively.

https://doi.org/10.1038/s41467-024-54557-8

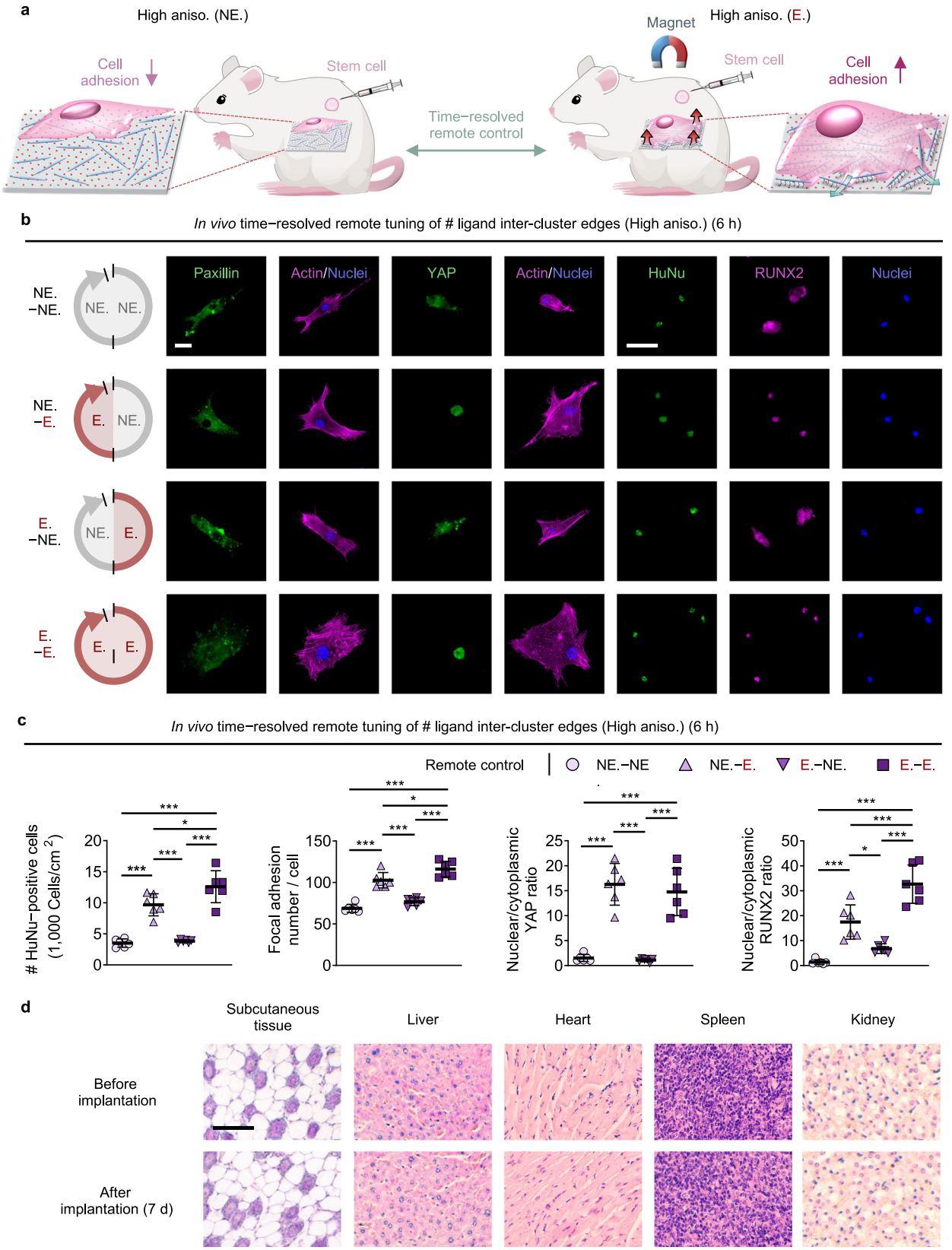

For the verification of in situ phase transformation of converting the akageneite phase (monoclinic structure) in anisotropic nano-blocker precursors into the magnetite phase (inverse spinel structure) during the reduction, in situ, TEM, HR-TEM, and selected area electron diffraction (SAD) imaging were performed by using a Titan™ 80-300. FFT analysis was also performed on the images (aligned along the zone axis) acquired from in situ HR-TEM imaging for the crystal structure analysis. The analyses of the phase transformation under anneal conditions at 340 °C for 2 h were performed using representative moderate-anisotropy nano-blocker precursors at an accelerating voltage of 200 kV with a heating rate of 0.45 °C/s. For the in situ SAD pattern, 60 frames were captured over 130 min and the resulting in situ

Fig. 9 | Time-resolved tuning of # ligand inter-cluster edges regulates stem cell behaviors in vivo. a Schematic illustration of the time-resolved elevation ("E.") and non-elevation ("NE.") control of high-anisotropy nano-blockers to tune # ligand inter-cluster edges in vivo for the regulation of injected stem cells on the implanted materials. **b** Immunostained fluorescent images of paxillin or YAP co-stained with F-actin and nuclei (DAPI), and HuNu co-stained with RUNX2 and nuclei (DAPI) of adherent stem cells after 6 h of injection onto the subcutaneously implanted material displaying a reversibly tunable # ligand inter-cluster edges. **c** Computation of the HuNu-positive cell density ($n = 6$ biological replicates; $^{*}p < 0.05$; $^{***}p < 0.001$), the focal adhesion number ($n = 6$ cells; $^{*}p < 0.05$; $^{***}p < 0.001$), and the nuclear/cytoplasmic intensity ratios of YAP and RUNX2 expression ($n = 6$ cells; $^{*}p < 0.05$; $^{***}p < 0.001$) in adherent stem cells after 6 h of injection. **d** Hematoxylin and eosin (H&E) stained images of subcutaneous tissue near the implanted site and major organs (liver, heart, spleen, and kidney) of mice before and 7 d after material implantation to assess the toxicity of implanted materials locally and systemically, respectively. A piece of permanent magnet was carefully coupled to the backs of the mice to direct the elevation of high-anisotropy nano-blockers in vivo. The coupling and uncoupling of the magnet were either switched or maintained after 3 h for 6 h ("NE.-NE.", "NE.-E.", "E.-NE.", and "E.-E."). Scale bars: 50 μm (confocal microscopy) and 200 μm (optical microscopy). Data are shown as the means ± standard errors. Statistical analysis was performed using one-way ANOVA along with the Tukey–Kramer post hoc test. Source data are provided as a Source Data file.

movie was produced at 780 times faster than in real-time speed. The distinctive rings of diffraction for the (310) plane corresponding to the akaganeite phase and the (220) plane corresponding to the magnetite phase were colored in turquoise and red, respectively.

In situ TEM analysis

For the examination of homogeneous shapes and sizes of the anisotropic nano-blocker precursors, anisotropic nano-blockers, and GNPs, TEM imaging was conducted with Talos G2 apparatus from Thermo Fisher[75]. Analysis of the obtained TEM images using ImageJ software allowed the computation of anisotropic nanorod length, width, anisotropy [calculated by dividing the nanorod length (major axis) by its width (minor axis)], and projected area.

In situ SAD analysis

For crystalline atomic structure characterizations, anisotropic nano-blocker precursors and anisotropic nano-blockers were characterized for the crystal structure verification of the akaganeite in the nano-blocker precursors and magnetite in the nano-blocker via SAD analysis using a Titan 80-300 with a camera length of 60 mm. The results were presented in the SAD pattern that showed multiple rings of diffraction corresponding to various planes, such as (200), (103), (211), (310), and (411) for the akaganeite phase and (220), (311), (400), (511), and (440) for the magnetite phase.

In situ HR-TEM analysis

The anisotropic nano-blocker precursors, anisotropic nano-blockers, and GNPs were characterized for the atomic structure visualizations of the akaganeite in the nano-blocker precursors, magnetite in the nano-blockers, and gold in GNPs via HR-TEM analysis using a Titan 80-300 apparatus at an accelerating voltage of 300 kV. The average d-spacing between the successive lattice planes (approximately 5.2–5.4 Å for akaganeite, 3.1 Å for magnetite, and 2.4 Å for gold) was measured and identified based on available data for the respective crystalline structures.

In situ FFT analysis

The images (aligned along the zone axis) acquired from HR-TEM imaging were exploited for the crystal structure analysis of the akaganeite phase in the nano-blocker precursors and the magnetite phase in the nano-blockers via FFT characterization. The results showed that periodic bright spots corresponded to the (200) plane of the akaganeite in the nano-blocker precursors and the (220) plane of the magnetite in the nano-blockers.

Linear profiles of elemental EDS mapping

For the structural and elemental analyses of anisotropic nano-blocker precursors and anisotropic nano-blockers, HAADF-STEM and EDS mapping were performed using the Talos G2 apparatus. HAADF-STEM imaging was carried out for the nanostructure examination of anisotropic nano-blocker precursors and anisotropic nano-blockers. The specific imaging conditions include a 200-kV acceleration voltage, a collection semi-angle of 38–200 mrad, a convergence semi-angle of 11.8 mrad, a pixel dwell time of 3 μs, a 1024 × 1024-pixel area, an electron probe size of 0.2 nm, an emission current of 185 μA, and a probe current of 185 pA.

EDS mapping and analyses (elemental spectra and line profile) of anisotropic nano-blocker precursors and anisotropic nano-blockers were conducted for the elemental composition (Fe, O, and Si elements) examination of the nanorods. The specific imaging was carried out at 200 kV and 2.13 nA with a speed of 15 min/image. The EDS mapping showed that Fe was present solely in the core, O was evenly distributed, and Si was solely present in the silica envelop of nano-blocker precursors and nano-blockers. The EDS line profiles, taken from the midsection of nano-blocker precursors and nano-blockers, confirmed individually optimized silica envelops for each varying anisotropy.

HR-STEM

The anisotropic nano-blockers and GNPs were subjected to HR-STEM characterization using Titan 80-300 apparatus for the atomic structure examinations of crystalline magnetite in the nano-blockers and gold in the GNPs. The imaging was performed at 300 kV with a Cs-corrected TM 80-300 probe at a magnification of 10 million times under conditions including 47.5–200-mrad collection semi-angle, 12-mrad convergence semi-angle, 8-μs pixel dwell time, 2048 × 2048 pixel area, 0.08-Å electron probe size, 197-μA emission current, and 62.5-pA probe current. The lattice parameters of the (100) plane of the magnetite (8.4 Å) and (111) planar spacing of the gold (2.4 Å) were calculated to confirm their respective crystalline structures.

XRD analysis

For the crystalline plane examination of the akaganeite in the nano-blocker precursors and magnetite in the nano-blockers, XRD analysis was performed using a D/MAX-2500V/PC apparatus from Rigaku with Cu Kα radiation. The typical diffraction peaks such as (103), (211), (310), (411), and (512) for the akaganeite phase and (220), (311), (400), (511), and (440) for the magnetite phase were identified for the respective crystalline planes.

Magnetic property analysis

For the examination of non-magnetic anisotropic nano-blocker precursor properties and magnetically reversible anisotropic nano-blocker properties, VSM measurement was conducted using an EV9-380 apparatus (Microsense). The measured magnetic moments were assessed as hysteresis loops under a magnetic field and presented after normalization to the respective dry weight of the material.

Amine-functionalization of anisotropic nano-blockers

For the versatile application of anisotropic nano-blockers, their silica envelops were functionalized with amine groups by mixing 10 mL of each nano-blocker in various anisotropies with 60 mL of ethanol. The suspension was mixed with 1 mL of (3-aminopropyl) triethoxysilane (APTES) and stirred at room temperature for 16 h. The resulting

anisotropic nano-blockers with amine-functionalized silica envelopes were washed with centrifugation using ethanol and then suspended in 40 mL of DI water.

Polymer linker-coupling of anisotropic nano-blockers

For the reversible tuning of the number of inter-cluster edges (referred to as "# inter-cluster edges"), nano-blockers in various anisotropies ("Low aniso. nano-blocker", "Moder. aniso. nano-blocker", and "High aniso. nano-blocker") were coated with polymer linkers. The procedure involved adding 0.5 mg of maleimide-poly(ethylene glycol)-*N*-hydroxy-succinimide (Mal-PEG-NHS, molecular weight of 10 kDa from Polysciences), 20 μL of phosphine hydrochloride (TCEP), and 2 μL of *N*, *N*-diisopropylethylamine (DIPEA) to 1 mL of amine-functionalized anisotropic nano-blockers, then vortexing the mixture for 16 h in the dark at 25 °C. This procedure produced polymer linker-coupled amine-functionalized anisotropic nano-blockers ready for grafting to the materials with the interconnected ligand nodes ("Low aniso.", "Moder. aniso.", and "High aniso.").

Zeta potential analysis

For the verification of the changes in the surface charge before and after coupling polymer linkers to the amine-functionalized anisotropic nano-blockers, zeta potential analysis was conducted using a Zetasizer Nano ZS90 apparatus from Malvern Panalytical.

FTIR analysis

For the verification of specific chemical bonds formed after the amine-functionalization and polymer linker-coupling of the anisotropic nano-blockers, FTIR analysis was conducted using a Nicolet iS10 apparatus from Thermo Fisher Scientific. Beforehand, samples in the suspension state were dried, embedded in KBr pellets, and measured for the FTIR. The absorption peaks were identified based on their matching with the chemical bonds of the anisotropic nano-blockers exhibiting Si-O and Fe-O bonds. The absorption peaks after the change in the chemical bond with identified at the peaks of O=C−NH and C−O bonds signifying the successful polymer linker-coupling.

Synthesis of the GNPs of distinctly different sizes

For the obvious discrimination of smaller GNPs acting as ligand nodes of the interconnected ligands on the material surface and larger GNPs utilized for tagging integrin β1 of the recruited stem cell, GNPs of distinctly different sizes were separately prepared. For their synthesis of smaller- and larger-sized GNPs, 20 mL of 1-mM hydrogen tetrachloroaurate (III) trihydrate ($HAuCl_4 \cdot 3H_2O$) was first shaken at 100 °C for 30 min. Followingly, 1.6 mL (for smaller GNPs in the diameter of 20 nm) or 2.5 mL (for larger GNPs in the diameter of 40 nm) of 38.8-mM trisodium citrate ($Na_3C_6H_5O_7$) was added and stirred for 15 min. The GNPs were each collected when the color of the solution changed from yellow to burgundy red, signifying the completion of the reaction.

DLS analysis

For the confirmation of homogeneous GNPs in smaller (in the diameter of 20 nm) and larger (in the diameter of 40 nm) sizes used in this study, a DLS examination was conducted with a Zetasizer Nano ZS90 apparatus from Malvern Panalytical.

Development of materials displaying a reversibly tunable number of inter-cluster edges within interconnected ligand networks

To develop materials displaying a reversibly tunable number of inter-cluster edges within interconnected ligand networks, the nano-blockers of each anisotropy were grafted via polymer linkers over the interconnected ligand nodes (liganded smaller GNPs) presented on the material surface. To decouple other parameters, the nano-blockers of each anisotropy were designed to exhibit similar projected areas, which were grafted to the material surface at similar density, enabling the variation of only anisotropy in the nano-blockers to present a tunable number of inter-cluster edges of interconnected ligands. To this end, glass coverslips (22 × 22 mm^2, cell culture grade) used as the material were sterilized by washing with a 1:1 hydrochloric-methanol solution for 45 min, followed by rinsing with DI water three times. Afterward, the coverslips were treated with sulfuric acid (H_2SO_4) for 70 min to activate their surface with hydroxyl (−OH) groups, followed by washing with DI water and methanol. The hydroxyl-activated surface was then thiolated for 70 min in a solution of (3-mercaptopropyl) trimethoxysilane (MPTMS) and ethanol (1:19) in the dark, followed by rinsing with ethanol and DI water and drying in an oven at 100 °C for 70 min.

To fabricate the interconnected ligand network, the thiolated surfaces of the materials were first incubated with 300 μL of smaller GNPs (in the diameter of 20 nm) at 25 °C for 16 h in the dark for their grafting through gold-thiol bonding. Successive treatment with a solution of 0.2 nM of thiolated RGD tripeptide ligand (CDD RGD from GI Biochem) and 10 mM of tris(2-carboxyethyl)phosphine (TCEP) for 12 h in the dark followed by DI water washing resulted in the material-grafted liganded GNPs via the gold-thiol bond, thereby turning them into completely interconnected ligand nodes. In this procedure, TCEP was used to prevent any non-specific grafting of the thiolated ligand to the thiolated surface through disulfide bonds.

The material surfaces exhibiting completely interconnected ligands were then incubated with 300 μL of polymer linker-coupled nano-blockers of each anisotropy for 16 h in the dark, followed by rinsing with DI water. The polymer linker-coupled anisotropic nano-blockers were grafted to the material surface not covered with the interconnected ligand nodes through maleimide-thiol bonding. The residual surfaces not covered with either the ligand nodes or anisotropic nano-blockers were treated with 2 mL of DI water containing 0.75 mg of methoxy-PEG-maleimide (MeO-PEG-Mal, molecular weight of 750 Da from Sigma–Aldrich) at 25 °C for 2 h in the dark to prevent non-specific cell adhesion to the non-liganded surfaces. The material surfaces were then washed with DI water.

To linearize the anisotropic nano-blockers ["Low aniso. (Lin.)", "Moder. aniso. (Lin.)", and "High aniso. (Lin.)"], the materials were subjected to three rounds of magnetic annealing for 15 min each during their incubation period with the polymer linker-coupled anisotropic nano-blockers. The uniform magnetic field produced by a 13.5-A electric current applied to the electromagnets at both ends of the materials linearized the anisotropic nano-blockers in the direction of the magnetic field. The magnetic annealing system was optimized so that the nano-blockers could be linearized without being attracted to the magnets. In our study, the anisotropic nano-blockers were assumed to be randomly oriented unless the linearization was stated.

Systematic analysis of tunable # ligand inter-cluster edges

The SEM imaging was conducted with a Quanta 250 FEG SEM (FEI) to examine the arrangement of the liganded GNPs (ligand nodes) and anisotropic nano-blockers on the material surface displaying reversibly tunable average number of inter-cluster edges within the interconnected ligand networks. Beforehand, the materials were dried under a vacuum and coated with platinum before SEM imaging. Analysis of the obtained SEM images using ImageJ software revealed a highly homogeneous arrangement of the ligand nodes with their similar values of inter-distance and surface density of the anisotropic nano-blockers, as well as different values of the average number of inter-cluster edges and the average inter-angle between the nano-blockers (in absolute value). The highly consistent regular distribution of the ligand nodes on the material surfaces allowed cells to sense them as interconnected ligands that could be analyzed to compute the average number of inter-cluster edges. Moreover, the identical surface

density of anisotropic nano-blockers in each group suggests the difference in the average number of inter-cluster edges in each group to be mainly attributed to the anisotropy difference of nano-blockers.

Analysis of the interconnected ligands using the average number of inter-cluster edges

To quantitatively analyze the interconnected ligand clusters, the notion of the average number of inter-cluster edges based on graph theory was utilized[76,77]. In our system, the liganded GNPs that each acted as ligand nodes were homogeneously arranged with equal inter-distances (approximately 200 nm). To facilitate graph theory-based analysis, the edges between ligand nodes were established using Delaunay triangulation, which ensures geometrically consistent connections between neighboring ligand nodes by maximizing the minimum angle of each triangle to achieve tessellation close to equilateral triangles[78,79]. Each liganded GNP node in the network structure in the SEM images was mapped as coordinates using ImageJ software, then connected by edges by applying Delaunay triangulation in Python. Following the construction of the ligand network, the edges that are disconnected by the presence of anisotropic nano-blockers were removed, resulting in the modeling of the ligand network involving anisotropic nano-blockers. Subsequently, these network models were partitioned into clusters by maximizing the modularity using the Louvain algorithm in Python. Finally, the average number of inter-cluster edges (referred to as "# inter-cluster edges") was calculated by dividing the number of interconnected edges between clusters by the number of connected cluster pairs. The "Low aniso.", "Moderate aniso.", and "High aniso." groups present different # inter-cluster edges of highly organized ligand nodes in the presence of anisotropic nano-blockers where the obstruction of connected edges between ligand clusters is stimulated with escalating nano-blocker anisotropy that reduces # inter-cluster edges. Remote control of irreversible linearization ("Lin.") of high-anisotropy nano-blockers yields their presentation in an ordered manner, resulting in more locally unobstructed ligand node connections and thus partly enhancing # inter-cluster edges as compared with the non-linearized group. Remote control of elevating anisotropic nano-blockers ("E.") reconnects the interconnected ligand nodes allowing cell infiltration under the elevated nano-blockers, which are disconnected in the presence of non-elevated nano-blockers ("NE."), resulting in a significant escalation of # inter-cluster edges.

Optimization of the polymer linker density to reversibly control # ligand inter-cluster edges

To confirm the optimized polymer linker density used to graft the anisotropic nano-blockers to the material surface that allows cells to sense the ligand nodes to be interconnected across the elevated anisotropic nano-blockers and thus infiltrate through the nano-gap under them, Ellman's assay was performed. To this end, each 20 μL of "High aniso. nano-blocker" (approximately 654 k nanorods per 1 μL) coupled with either a low (150 μg) or high (6000 μg) amount of polymer linker was first reacted four times independently with 3.6 μg of thiolated L-cysteine via thiol-ene bond at room temperature. Successive applications of Ellman's assay enabled a comparative analysis of the density of polymer linkers coupled on each nano-blocker by computing the concentration of L-cysteine reacted with the polymer linkers coupled to the nano-blockers, in which a high number of reacted L-cysteine signified high density of polymer linkers coupled on the nano-blockers. For such calculation, the amount of unreacted L-cysteine determined by the amount of residual Ellman's reagent in the supernatant was subtracted from the total amount of added L-cysteine. SEM images of the IGNP tagging of recruited integrin in stem cells confirmed that the low density of polymer linkers used to graft the nano-blockers to the materials ("High aniso.") was optimized for cells to infiltrate under the elevated nano-blockers, while the high density of polymer linkers blocked the cell infiltration albeit under the elevated state.

In situ imaging of the cyclic remote control of the anisotropic nano-blocker

For the examination of cyclic remote control of anisotropic nano-blockers on the materials enabling reversibly tunable # inter-cluster edges of interconnected ligands, AFM was performed with an XE-100 System from Asylum Research at room temperature in air mode using an SSS-SEIHR-20 AFM cantilever (spring constant: 5–37 N/m, resonance frequency: 96–175 kHz) from Nanosensors. The remote modulation of the anisotropic nano-blockers situated over the interconnected ligand nodes (liganded smaller GNPs in the diameter of 20 nm) that reversibly controls their # inter-cluster edges was examined via peak height change. The application of an upward magnetic field pulls the anisotropic nano-blockers away from the ligand nodes situated under them, thereby escalating # ligand inter-cluster edges by reconnecting the ligand nodes that were originally inaccessible to cells. In the absence of the magnetic field, anisotropic nano-blockers obstruct the interconnection of ligands reducing # ligand inter-cluster edges.

The identical area of the "High aniso." material displaying nano-blockers in high-anisotropy over smaller GNPs was cyclically imaged underemployment ("E.") and non-employment ("NE.") a piece of permanent magnet (295 mT) above the material. The differences in linear height profile and the computed peak height of the high-anisotropy nano-blockers between the elevated ["High aniso. (E.)"] and non-elevated ["High aniso. (NE.)"] states were analyzed by using the Igor Pro 6.12 A and ImageJ software to verify the cyclic tuning of # inter-cluster edges of interconnected ligands in situ.

Stem cell regulation by tuning # ligand inter-cluster edges only

The materials displaying reversibly tunable # inter-cluster edges of interconnected ligand networks were first sterilized for 3 h via UV light irradiation. They were employed to culture human mesenchymal stem cells (hMSCs, passage 5) provided and authenticated by Lonza (catalog number: PT-2501) to probe the effect of tuning # ligand inter-cluster edges on integrin recruitment, focal adhesion, mechanotransduction, and following differentiation. Owing to the relatively large size of stem cells on the hundreds of micrometer scale, they were employed as a model cell type whose responses to materials can be systematically analyzed via the average # ligand inter-cluster edges that can be generalized for microscale ligand modeling by calculating the number of connected edges between ligand clusters for each ligand cluster pair in SEM images.

In specific, to probe the effect of # ligand inter-cluster edges on stem cell adhesion, stem cells (100k cells per cm^2) were seeded only at the initial stage of culture (without additions at the later stage) onto the materials under the conditions of 37 °C and 5% CO_2 using growth medium prepared by supplementing 10% fetal bovine serum (FBS), 4 mM L-glutamine, and 50 U/mL of penicillin and streptomycin into high glucose Dulbecco's modified Eagle medium (DMEM). To this end, each material displays nano-blockers of different anisotropy ("Low aniso.", "Moder. aniso.", and "High aniso.") and linearized nano-blockers ["High aniso. (Lin.)"] were used to assess the adherent stem cells after 48 h of culturing. To verify the # RGD ligand inter-cluster edges-specific regulation of stem cells, the following control groups were employed: "Non-decorated material", "GNP-decorated material", "Liganded GNP-decorated material", "Low aniso. free of ligand", "Moder. aniso. free of ligand", and "High aniso. free of ligand". To compare the effectiveness of stem cell regulation by ligand ordering, the following control groups were employed: both non-linearized and linearized nano-blockers of different anisotropy including "Low aniso.", "Low aniso. (Lin.)", "Moder. aniso.", and "Moder. aniso. (Lin.)" groups.

Regulation of stem cell behaviors via cyclic tuning of # ligand inter-cluster edges

Cyclic tuning of # ligand inter-cluster edges was achieved by controlling the elevation of anisotropic nano-blockers was analyzed for the

adherent cells after 72 h of culturing on each material displaying anisotropic nano-blockers with the employment "High aniso. (E.)" or the non-employment "High aniso. (NE.)" of a piece of permanent magnet (295 mT) above the materials that were switched or maintained after every 24 h up to 72 h for the "High aniso." group ("NE.-NE.-NE.", "NE.-E.-NE.", "E.-NE.-E.", and "E.-E.-E."). To compare the effectiveness of stem cell adhesion by manipulating the elevation of the nano-blockers, the following control groups were employed: both low-anisotropy and moderate-anisotropy nano-blockers including "Low aniso. (E.)", "Low aniso. (NE.)", "Moder. aniso. (E.)", and "Moder. aniso. (NE.)" groups.

Cycling tuning of # ligand inter-cluster edges was also applied to evaluate its effect on the mechanosensing and differentiation of stem cells by culturing them in osteogenic differentiation medium, which was prepared by supplementing 100 nM of dexamethasone, 50 μM of ascorbic acid-2-phosphate, and 10 mM of glycerophosphate into the growth medium, using all the other experimental conditions and groups used in the adhesion experiments.

Regulation of mechanotransduction-mediated stem cell differentiation via tuning # ligand inter-cluster edges was probed either at 48 h (mechanotransduction) or 72 h (differentiation) after culturing in a growth medium or osteogenic differentiation medium, respectively. Each medium used in both conditions was supplemented with one of the following cell adhesion-related inhibitors: ML9 (myosin II-inhibitor, 0.1 μM), Swinholide A (actin polymerization-inhibitor, 0.1 μM), or Y27632 [ROCK-inhibitor, 50 μM] or none for the control group.

Fluorescent immunostaining and quantification analysis

For the investigation of the stem cell-regulatory effect of tuning # ligand inter-cluster edges, fluorescent immunostaining was carried out. Stem cells after culture were fixed in 4% paraformaldehyde (PFA) at room temperature for 10 min, followed by washing with PBS three times. The fixed cells were then blocked using a blocking buffer (3% bovine serum albumin (BSA) and 0.1% Triton X in PBS) at 37 °C for 40 min. The blocked cells were then treated with a blocking buffer containing primary antibodies [Paxilin (Santa Cruz, sc-365379), integrin β1 (Santa Cruz, sc-374429), YAP (Santa Cruz, sc-101199), RUNX2 (Abcam, ab192256), and HuNu (Sigma–Aldrich, MAB1281)] and then incubated at 4 °C for 16 h, followed by washing with 0.5% Tween 20 in PBS four times. The cells were serially incubated in a blocking buffer containing fluorescent secondary antibodies [Alexa Fluor 488 (Thermo Fisher, A11001 and A21206), and Alexa Fluor 546 (Thermo Fisher, A11030)] and phalloidin (Thermo Fisher, A12379) at room temperature for 45 min in the dark, washed four times with 0.5% Tween 20 in PBS, and then immersed in DAPI (Thermo Fisher, P36931) antifade solution.

For the analysis of fluorescently immunostained stem cells, imaging was performed with an LSM700 confocal microscope and Lattcie SIM 5 (NFEC-2024-11-301127) both from Carl Zeiss using the same laser exposure conditions for all groups. Using the confocal images, ImageJ software was utilized to compute the density of adherent stem cells (calculating the number of DAPI-positive nuclei per unit area), the number of focal adhesions per cell (calculating the number of paxillin-positive clusters larger than 1 μm^2 in each cell), the area per cell (actin-positive area), and the aspect ratio (the longest length divided by the shortest length) of adhered cells[80]. The fluorescence intensities of integrin β1 and the nuclear/cytoplasmic ratios of YAP and RUNX2 fluorescence intensities were determined by analyzing integrin β1-stained images or YAP- or RUNX2-stained images along with the co-staining of phalloidin and DAPI.

For the quantitative analysis of stem cell differentiation, western blotting analysis was conducted after 72 h of cell culturing under the cyclic tuning of # ligand inter-cluster edges in the "High aniso." group. The proteins of interest in the adherent cells, RUNX2 (Santa Cruz, sc-101145, 60 kDa) and ALP (Abcam, ab67228, 75 kDa), were extracted via centrifugation using PRO-PREPTM solution (iNtRON Biotechnology) and a protease-inhibitor. After mixing with loading dye and denaturing, protein quantification was performed using a BCA Protein Assay Kit from Thermo Scientific. Denatured proteins were separated on 10% sodium dodecyl sulfate (SDS)-polyacrylamide gel electrophoresis (PAGE) gels at 110 V for 1 h and then electroblotted onto polyvinylidene difluoride (PVDF) membranes at 120 V for 1.5 h. The membranes were serially blocked with TBST blocking buffer (5% skimmed milk) for 1 h, incubated with primary antibodies (RUNX2, ALP, and GAPDH) for 16 h, washed with TBST buffer, and then incubated with secondary antibodies conjugated with anti-horse radish peroxidase. Protein expression was visualized and computed using a Linear Image Quant LAS 4000 mini chemiluminescent imaging system after normalization to GAPDH expression. The levels of RUNX2 and ALP protein expressions were determined relative to GAPDH (Santa Cruz, sc-365062, 37 kDa) as an internal control using a chemiluminescent imaging system.

IGNP tagging of recruited integrin

For the examination of stem cell integrin β1 recruitment to the interconnected ligand nodes depending on their tunable # inter-cluster edges, IGNP tagging with analysis was performed. For their obvious discrimination in SEM imaging from smaller GNPs (in the diameter of 20 nm) that act as the ligand nodes, homogeneous larger GNPs (in the diameter of 40 nm) were used for IGNP tagging. To allow larger GNPs for tagging stem cell integrins, they were first treated with a buffer (1% BSA, and 0.1% Tween 20 added to 0.1 M of 1,4 piperazine bis (2-ethanosulfonic acid) (PIPES) buffer at pH 7.4) containing secondary antibodies [goat anti-mouse (H+L) IgG (Abcam, ab6708)] under mild shaking at 37 °C for 16 h.

The adherent stem cells on the materials of different groups were washed with PIPES buffer, fixed in 4% PFA for 10 min, and washed with PBS. The fixed cells were then permeabilized with 0.5% Triton X-100, blocked with 1% BSA for 1 h, treated with integrin β1 primary antibodies at 37 °C for 1 h, and washed six times with 1% BSA. Consequent treatment of the integrin β1 primary antibody-treated cells with secondary antibody-conjugated IGNPs for 16 h allowed the IGNPs to bind to integrin, thereby tagging it in the stem cells. The cells were then washed with PIPES buffer and fixed with 2.5% glutaraldehyde for 7 min. To enhance the contrast for their clear visualization in SEM images, the cells were further treated with 1% osmium tetroxide, washed with PIPES buffer, filtered with DI water, and dried at 37 °C for 1 h.

For the analysis of cellular integrins recruited to the interconnected ligand nodes depending on # inter-cluster edges, the resulting IGNP-tagged stem cells were subjected to SEM imaging using FEI TENEO VS and EDS mapping (for Fe element in nano-blocker core) using an EDAX Octane Elect Super EDS System. Representative analysis of the former enabled the precise visualization of the recruited stem cell integrins to the ligand nodes on the materials, while the latter confirmed the presence and arrangement of the anisotropic nano-blockers that alter # inter-cluster edges of interconnected ligand nodes. The images of cells infiltrating under the elevated high-anisotropy nano-blockers ["High aniso. (E.)"] confirmed that cells sense the ligand nodes to be interconnected across the elevated anisotropic nano-blockers (low polymer linker density), which escalates the overall # ligand inter-cluster edges accessible by cells. For their clear identification in the acquired images, stem cells and IGNPs were each colored green and white, respectively. The average number of IGNPs-tagged integrin of stem cells at the cell boundary was calculated per unit area (μm^2).

In vivo stem cell regulation via time-resolved tuning of # ligand inter-cluster edges

40 male BALB/c nude mice (8-week-old) were used in the investigation of the effect of modulating # ligand inter-cluster edges on the focal adhesion, mechanosensing, and following differentiation of stem cells in vivo. Each mouse was first anesthetized via intraperitoneal injection of 60 μL of mixture (alfaxan and rompun in 3:1 ratio) after which an

incision was made on their backs, the prepared material implanted in a subcutaneous pocket, and then sutured. The materials (12×12-mm^2 glass) displaying reversibly tunable # inter-cluster edges of interconnected ligands were implanted into the subcutaneous pockets of mice. For such implantation, tweezers were used to lift the subcutaneous tissues and carefully implant the materials so that the surface displaying reversibly tunable # inter-cluster edges of interconnected ligands would face upward. Stem cells (300 k hMSCs per the implant) were then injected onto the implanted material surface and the mice were kept anesthetized for 6 h to immobilize them to ensure stable adherence of the stem cells to the materials without any breakage and leakage. A piece of permanent magnet (295 mT) was coupled to the backs of the mice using a bandage to elevate high-anisotropy nano-blockers ["High aniso. (E.)"] in vivo. The coupling and uncoupling were either switched or maintained after 3 h ("NE.-NE.", "NE.-E.", "E.-NE.", and "E.-E."). After implantation for 6 h, the mice were sacrificed and the implants were retrieved by carefully opening up the suture with operating scissors and picking up the materials using tweezers, followed by washing with PBS three times for the fluorescent immunostaining analysis of confirming adherent stem cells [human-specific nuclei antigen (HuNu)], focal adhesion, mechanosensing, and their following differentiation. The implants were also retrieved after 24 h for SEM imaging to validate in vivo preservation of the anisotropic nano-blockers and the liganded GNPs on the material surfaces after remote tuning of # inter-cluster edges of the interconnected ligands.

Local and systemic toxicity evaluation of the materials displaying reversibly tunable # ligand inter-cluster edges

For the assessment of the local and systemic toxicity, histological analysis was conducted on subcutaneous tissue collected near the implanted site and the major organs (liver, heart, spleen, and kidney) of the mice before and 7 d after implantation. The collected tissues and organs were first fixed in 4% PFA for 2 d and then washed three times with DI water. Before being embedded in paraffin at 62 °C for 16 h, the samples were sequentially dehydrated with increasing concentrations of ethanol (50%, 75%, 90%, 95%, and 100%) for 1 h each. After embedding, a HistoCore Multicut microtome from Leica RM2125 RTS Biosystem was used to cut the samples into 6 µm-thick sections for mounting onto glass slides. The sections were deparaffinized and rehydrated, then stained with hematoxylin and eosin (H&E) for the visualization of cellular structures within the extracellular matrix in tissues and organs. Nikon Eclipse Ts2 optical microscopy was used to examine the stained samples. The results showed that the materials displaying reversibly tunable # ligand inter-cluster edges inflicted inappreciable local and systemic toxicity.

Statistics and reproducibility

The results reported in this study were validated by independently repeating all experiments at least three times to ensure the production of consistent datasets. The computation of the data was performed using GraphPad Prism software (version 8.0.2). One-way analysis of variance (ANOVA) along with the Tukey–Kramer post hoc test is used to compare multiple groups and determine statistical significance. The level of significance is indicated by asterisks next to the p-values ($^*p < 0.05$, $^{**}p < 0.01$, and $^{***}p < 0.001$). The number of replicates in each experiment is represented by the "n" value.

Reporting summary

Further information on research design is available in the Nature Portfolio Reporting Summary linked to this article.

Data availability

All data generated in this study are provided in the Supplementary Information. Source data are provided with this paper.

Code availability

The code to establish the edges between ligand nodes (Delaunay triangulation) and partition the ligand network models into clusters (Louvain algorithm) is available at https://github.com/NayeonKang222/Kanglab2024-Ligand-Inter-Nanocluster-Connectivity-publish.

References

1. Ricard-Blum, S. Extracellular matrix networks: from connections to functions. *Extracellular Matrix Omics* 101–129 (Springer, Cham, 2020).
2. Ghiasi, M. S., Chen, J., Vaziri, A., Rodriguez, E. K. & Nazarian, A. Bone fracture healing in mechanobiological modeling: a review of principles and methods. *Bone Rep.* **6**, 87–100 (2017).
3. Wang, T. et al. Engineering immunomodulatory and osteoinductive implant surfaces via mussel adhesion-mediated ion coordination and molecular clicking. *Nat. Commun.* **13**, 160 (2022).
4. Wei, Y. et al. Aligned cryogel fibers incorporated 3D printed scaffold effectively facilitates bone regeneration by enhancing cell recruitment and function. *Sci. Adv.* **10**, eadk6722 (2024).
5. Kannus, P. Structure of the tendon connective tissue. *Scand. J. Med. Sci.* **10**, 312–320 (2000).
6. Winkler, J., Abisoye-Ogunniyan, A., Metcalf, K. J. & Werb, Z. Concepts of extracellular matrix remodelling in tumour progression and metastasis. *Nat. Commun.* **11**, 5120 (2020).
7. Greene, C. S. et al. Understanding multicellular function and disease with human tissue-specific networks. *Nat. Genet.* **47**, 569–576 (2015).
8. Fujiu, K. et al. A heart–brain–kidney network controls adaptation to cardiac stress through tissue macrophage activation. *Nat. Med.* **23**, 611–622 (2017).
9. Cao, S. Z. et al. Inversely engineered biomimetic flexible network scaffolds for soft tissue regeneration. *Sci. Adv.* **9**, eadi8606 (2023).
10. Nguyen, T.-H., Eichmann, A., Le Noble, F. & Fleury, V. Dynamics of vascular branching morphogenesis: the effect of blood and tissue flow. *Phys. Rev. E* **73**, 061907 (2006).
11. Bosshardt, D. D. & Sculean, A. Does periodontal tissue regeneration really work? *Periodontol 2000* **51**, 208–219 (2009).
12. Weber, M. T., Arena, J. D., Xiao, R., Wolf, J. A. & Johnson, V. E. CLARITY reveals a more protracted temporal course of axon swelling and disconnection than previously described following traumatic brain injury. *Brain Pathol.* **29**, 437–450 (2019).
13. Kim, S. J., Park, Y. D. & Pillai, J. What is the fate of disconnected brain tissue in a child with Rasmussen syndrome? A case report. *Neuroradiology* **45**, 250–252 (2003).
14. Guggisberg, A. G. et al. Mapping functional connectivity in patients with brain lesions. *Ann. Neurol.* **63**, 193–203 (2008).
15. Vining, K. H. & Mooney, D. J. Mechanical forces direct stem cell behaviour in development and regeneration. *Nat. Rev. Mol. Cell Biol.* **18**, 728–742 (2017).
16. Li, J. et al. Intrapericardial hydrogel injection generates high cell retention and augments therapeutic effects of mesenchymal stem cells in myocardial infarction. *Chem. Eng. J.* **427**, 131581 (2022).
17. Wu, S. et al. Electrospun conductive nanofiber yarns for accelerating mesenchymal stem cells differentiation and maturation into Schwann cell-like cells under a combination of electrical stimulation and chemical induction. *Acta Biomater.* **139**, 91–104 (2022).
18. Zhao, Q., Wang, M., Duan, B., Kong, T. & Wang, C. Responsive biomaterials for tissue regeneration. *Front. Mater.* **9**, 880973 (2022).
19. Li, Y. et al. Expansion of human megakaryocyte-biased hematopoietic stem cells by biomimetic Microniche. *Nat. Commun.* **14**, 2207 (2023).
20. Li, H. et al. Targeted cell therapy for partial-thickness cartilage defects using membrane modified mesenchymal stem cells by transglutaminase 2. *Biomaterials* **275**, 120994 (2021).

21. Jiang, W. et al. Emergence of complexity in hierarchically organized chiral particles. *Science* **368**, 642–648 (2020).
22. Bullmore, E. & Sporns, O. Complex brain networks: graph theoretical analysis of structural and functional systems. *Nat. Rev. Neurosci.* **10**, 186–198 (2009).
23. Lee, M. D. et al. Small-world connectivity dictates collective endothelial cell signaling. *Proc. Natl Acad. Sci. USA* **119**, e2118927119 (2022).
24. Blondel, V. D., Guillaume, J. L., Lambiotte, R. & Lefebvre, E. Fast unfolding of communities in large networks. *J. Stat. Mech. Theory Exp.* **10**, P10008 (2008).
25. Guarracino, A. et al. Recombination between heterologous human acrocentric chromosomes. *Nature* **617**, 335 (2023).
26. Di Bella, D. J. et al. Molecular logic of cellular diversification in the mouse cerebral cortex. *Nature* **595**, 554 (2021).
27. Zhang, M. et al. Controllable ligand spacing stimulates cellular mechanotransduction and promotes stem cell osteogenic differentiation on soft hydrogels. *Biomaterials* **268**, 120543 (2021).
28. von Erlach, T. C. et al. Cell-geometry-dependent changes in plasma membrane order direct stem cell signalling and fate. *Nat. Mater.* **17**, 237 (2018).
29. Wang, X., Li, S. Y., Yan, C., Liu, P. & Ding, J. D. Fabrication of RGD micro/nanopattern and corresponding study of stem cell differentiation. *Nano Lett.* **15**, 1457–1467 (2015).
30. Conway, A. et al. Multivalent ligands control stem cell behaviour in vitro and in vivo. *Nat. Nanotechnol.* **8**, 831–838 (2013).
31. Koo, L. Y., Irvine, D. J., Mayes, A. M., Lauffenburger, D. A. & Griffith, L. G. Co-regulation of cell adhesion by nanoscale RGD organization and mechanical stimulus. *J. Cell Sci.* **115**, 1423–1433 (2002).
32. Changede, R., Cai, H., Wind, S. J. & Sheetz, M. P. Integrin nanoclusters can bridge thin matrix fibres to form cell–matrix adhesions. *Nat. Mater.* **18**, 1366–1375 (2019).
33. Zhu, Y. et al. Regulation of macrophage polarization through surface topography design to facilitate implant-to-bone osteointegration. *Sci. Adv.* **7**, eabf6654 (2021).
34. Yang, L. et al. A biodegradable hybrid inorganic nanoscaffold for advanced stem cell therapy. *Nat. Commun.* **9**, 3147 (2018).
35. Chen, Z. et al. Mechanical signal-tailored hydrogel microspheres recruit and train stem cells for precise differentiation. *Adv. Mater.* **35**, 2300180 (2023).
36. Gjorevski, N. et al. Tissue geometry drives deterministic organoid patterning. *Science* **375**, eaaw9021 (2022).
37. Kim, Y. et al. Remote active control of nanoengineered materials for dynamic nanobiomedical engineering. *View* **1**, 20200029 (2020).
38. Cheng, K. et al. Magnetic targeting enhances engraftment and functional benefit of iron-labeled cardiosphere-derived cells in myocardial infarction. *Circ. Res.* **106**, 1570–1581 (2010).
39. Kim, J. et al. In situ self-assembly for cancer therapy and imaging. *Nat. Rev. Mater.* **8**, 710–725 (2023).
40. Lee, T. T. et al. Light-triggered in vivo activation of adhesive peptides regulates cell adhesion, inflammation and vascularization of biomaterials. *Nat. Mater.* **14**, 352–360 (2015).
41. Kim, Y. et al. Photoswitchable microgels for dynamic macrophage modulation. *Adv. Mater.* **34**, 2205498 (2022).
42. Shadish, J. A., Benuska, G. M. & Deforest, C. A. Bioactive site-specifically modified proteins for 4D patterning of gel biomaterials. *Nat. Mater.* **18**, 1005–1014 (2019).
43. Zhang, C. et al. Semiconducting polymer nano-PROTACs for activatable photo-immunometabolic cancer therapy. *Nat. Commun.* **12**, 2934 (2021).
44. Wang, S. et al. Programmed degradation of a hierarchical nanoparticle with redox and light responsivity for self-activated photochemical enhanced chemodynamic therapy. *Biomaterials* **224**, 119498 (2019).
45. Kang, N. et al. Stimuli-responsive ferroptosis for cancer therapy. *Chem. Soc. Rev.* **52**, 3955–3972 (2023).
46. Lee, J.-U. et al. Non-contact long-range magnetic stimulation of mechanosensitive ion channels in freely moving animals. *Nat. Mater.* **20**, 1029–1036 (2021).
47. Wang, F., Pu, K. & Li, J. Activating nanomedicines with electromagnetic energy for deep-tissue induction of immunogenic cell death in cancer immunotherapy. *Small Methods* **7**, 2201083 (2023).
48. Prothmann, M. et al. High spatial resolution cardiovascular magnetic resonance at 7.0 tesla in patients with hypertrophic cardiomyopathy - first experiences: lesson learned from 7.0 tesla. *PLoS ONE* **11**, e0148066 (2016).
49. Yun, S. et al. Design of magnetically labeled cells (Mag-Cells) for in vivo control of stem cell migration and differentiation. *Nano Lett.* **18**, 838–845 (2018).
50. Li, W., Yan, Z., Ren, J. & Qu, X. Manipulating cell fate: dynamic control of cell behaviors on functional platforms. *Chem. Soc. Rev.* **47**, 8639–8684 (2018).
51. Min, S. et al. Remote control of time-regulated stretching of ligand-presenting nanocoils in situ regulates the cyclic adhesion and differentiation of stem cells. *Adv. Mater.* **33**, 2008353 (2021).
52. Min, S. et al. Independent tuning of nano-ligand frequency and sequences regulates the adhesion and differentiation of stem cells. *Adv. Mater.* **32**, 2004300 (2020).
53. Kim, J. S. et al. Critical roles of metal–ligand complexes in the controlled synthesis of various metal nanoclusters. *Nat. Commun.* **14**, 3201 (2023).
54. Gudzenko, T. & Franz, C. M. Studying early stages of fibronectin fibrillogenesis in living cells by atomic force microscopy. *Mol. Biol. Cell* **26**, 3190–3204 (2015).
55. Khatua, C. et al. In situ magnetic control of macroscale nanoligand density regulates the adhesion and differentiation of stem cells. *Nano Lett.* https://doi.org/10.1021/acs.nanolett.1020c00559 (2020).
56. Sibson, R. Locally equiangular triangulations. *Comput. J.* **21**, 243–245 (1978).
57. Stolz, B. J. et al. Multiscale topology characterizes dynamic tumor vascular networks. *Sci. Adv.* **8**, eabm2456 (2022).
58. Saraswathibhatla, A., Indana, D. & Chaudhuri, O. Cell–extracellular matrix mechanotransduction in 3D. *Nat. Rev. Mol. Cell Biol.* **24**, 1–22 (2023).
59. Adebowale, K. et al. Enhanced substrate stress relaxation promotes filopodia-mediated cell migration. *Nat. Mater.* **20**, 1290–1299 (2021).
60. Higgins, S. G. et al. High-aspect-ratio nanostructured surfaces as biological metamaterials. *Adv. Mater.* **32**, 1903862 (2020).
61. Li, X. et al. A nanostructure platform for live-cell manipulation of membrane curvature. *Nat. Protoc.* **14**, 1772–1802 (2019).
62. Capozza, R. et al. Cell membrane disruption by vertical micro-/nanopillars: role of membrane bending and traction forces. *ACS Appl. Mater. Interfaces* **10**, 29107–29114 (2018).
63. Hansel, C. S. et al. Nanoneedle-mediated stimulation of cell mechanotransduction machinery. *ACS Nano* **13**, 2913–2926 (2019).
64. Trappmann, B. et al. Extracellular-matrix tethering regulates stem-cell fate. *Nat. Mater.* **11**, 642–649 (2012).
65. Attwood, S. J. et al. Adhesive ligand tether length affects the size and length of focal adhesions and influences cell spreading and attachment. *Sci. Rep.* **6**, 34334 (2016).
66. Popkova, A. et al. A Cdc42-mediated supracellular network drives polarized forces and Drosophila egg chamber extension. *Nat. Commun.* **11**, 1921 (2020).
67. Shin, J. et al. One-dimensional nanomaterials for cancer therapy and diagnosis. *Chem. Soc. Rev.* **52**, 4488–4514 (2023).
68. Meyen, D. et al. Dynamic filopodia are required for chemokine-dependent intracellular polarization during guided cell migration in vivo. *eLife* **4**, e05279 (2015).
69. Maier-Hauff, K. et al. Efficacy and safety of intratumoral thermotherapy using magnetic iron-oxide nanoparticles combined with

external beam radiotherapy on patients with recurrent glioblastoma multiforme. *J. Neurooncol.* **103**, 317–324 (2011).
70. Lanniel, M. et al. Substrate induced differentiation of human mesenchymal stem cells on hydrogels with modified surface chemistry and controlled modulus. *Soft Matter* **7**, 6501–6514 (2011).
71. Zhao, W., Li, X. W., Liu, X. Y., Zhang, N. & Wen, X. J. Effects of substrate stiffness on adipogenic and osteogenic differentiation of human mesenchymal stem cells. *Mater. Sci. Eng. C.* **40**, 316–323 (2014).
72. Das, A., Monteiro, M., Barai, A., Kumar, S. & Sen, S. MMP proteolytic activity regulates cancer invasiveness by modulating integrins. *Sci. Rep.* **7**, 14219 (2017).
73. Butler, K. T., Davies, D. W., Cartwright, H., Isayev, O. & Walsh, A. Machine learning for molecular and materials science. *Nature* **559**, 547–555 (2018).
74. Batra, R., Song, L. & Ramprasad, R. Emerging materials intelligence ecosystems propelled by machine learning. *Nat. Rev. Mater.* **6**, 655–678 (2021).
75. Kim, Y. et al. Submolecular ligand size and spacing for cell adhesion. *Adv. Mater.* **34**, 2110340 (2022).
76. Chodrow, P. S., Veldt, N. & Benson, A. R. Generative hypergraph clustering: from blockmodels to modularity. *Sci. Adv.* **7**, eabh1303 (2021).
77. Yamamoto, H. et al. Modular architecture facilitates noise-driven control of synchrony in neuronal networks. *Sci. Adv.* **9**, eade1755 (2023).
78. Scholaert, M. et al. 3D deconvolution of human skin immune architecture with multiplex annotated tissue imaging system. *Sci. Adv.* **9**, eadf9491 (2023).
79. Zakharov, A. et al. Clots reveal anomalous elastic behavior of fiber networks. *Sci. Adv.* **10**, eadh1265 (2024).
80. Deeg, J. A. et al. Impact of local versus global ligand density on cellular adhesion. *Nano Lett.* **11**, 1469–1476 (2011).

Acknowledgements

This work was supported by the National Research Foundation of Korea (NRF) grant funded by the Korean government (MSIT) (No. RS-2023-00208427 to H.K.), the Basic Science Research Program through the National Research Foundation of Korea (NRF) funded by the Ministry of Education (No. 2022R1A6A3A13071324 to S.M.), and a Korea University Grant. Y.S.Z. further acknowledges the support by the Chan Zuckerberg Initiative (2022-316712) and the Brigham Research Institute.

Author contributions

C.K., N.K., Y.S.Z., and H.K. conceived and designed the experiments. C.K., N.K., S.M., R.T., S.L., H.H., K.K., S.Y.K., D.K., H.R., K.-R.T., H.-J.L., N.S., D.J., J.H., Y.K., and S.P. performed the experiments. H.L., T.K., S.W.S., S.P., S.K., Y.Z., A.H.N., Z.C., W.S., P.Z., K.Z., L.B., H.-C.S., S.-G.P., J.S.K., S.-Y.L., J.-P.A., H.-K.K., Y.S.Z., and H.K. analyzed the data. Y.S.Z. and H.K. wrote the manuscript.

Competing interests

Y.S.Z. consulted for Allevi by 3D Systems, sits on the scientific advisory board, and holds options of Xellar, neither of which, however, participated in or biased the work. All other authors declare no competing interests.

Additional information

Supplementary information The online version contains supplementary material available at https://doi.org/10.1038/s41467-024-54557-8.

Correspondence and requests for materials should be addressed to Yu Shrike Zhang or Heemin Kang.

Peer review information *Nature Communications* thanks Kenichiro Kamei, and the other, anonymous, reviewers for their contribution to the peer review of this work. A peer review file is available.

Reprints and permissions information is available at http://www.nature.com/reprints

Publisher's note Springer Nature remains neutral with regard to jurisdictional claims in published maps and institutional affiliations.

[1]Department of Materials Science and Engineering, Korea University, Seoul, Republic of Korea. [2]Advanced Analysis Center, Korea Institute of Science and Technology (KIST), Seoul, Republic of Korea. [3]Department of Chemistry, Korea University, Seoul, Republic of Korea. [4]Department of Orthopedic Surgery, Korea University Anam Hospital, Seoul, Republic of Korea. [5]Department of Chemical and Biomolecular Engineering, Yonsei University, Seoul, Republic of Korea. [6]Nano-Bio Convergence Department, Korea Institute of Materials Science (KIMS), Changwon, Gyeongnam, Republic of Korea. [7]Department of Future Convergence Materials, Korea University, Seoul, Republic of Korea. [8]Department of Dermatology, Korea University Ansan Hospital, Korea University College of Medicine, Ansan, Republic of Korea. [9]Department of Materials Science and Engineering, Korea Advanced Institute of Science and Technology (KAIST), Daejeon, Republic of Korea. [10]Terasaki Institute for Biomedical Innovation, Los Angeles, CA, USA. [11]Department of Electrical and Electronic Engineering, Joint Appointment with School of Biomedical Sciences, The University of Hong Kong, Hong Kong, PR China. [12]Department of Biological Systems Engineering, Virginia Tech, Blacksburg, VA, USA. [13]School of Biomedical Sciences and Engineering, Guangzhou International Campus, South China University of Technology, Guangzhou, PR China. [14]Electronic Materials Research Center, Korea Institute of Science and Technology (KIST), Seoul, Republic of Korea. [15]KIST-SKKU Carbon-Neutral Research Center, Sungkyunkwan University (SKKU), Suwon, Republic of Korea. [16]Division of Engineering in Medicine, Department of Medicine, Brigham and Women's Hospital Harvard Medical School, Cambridge, MA, USA. [17]College of Medicine, Korea University, Seoul, Republic of Korea. [18]These authors contributed equally: Chowon Kim, Nayeon Kang. ✉e-mail: yszhang@bwh.harvard.edu; heeminkang@korea.ac.kr